

# The *Virga-Sniffer* - a new tool to identify precipitation evaporation using ground-based remote-sensing observations

Heike Kalesse-Los<sup>1,\*</sup>, Anton Kötsche<sup>1</sup>, Andreas Foth<sup>1</sup>, Johannes Röttenbacher<sup>1</sup>, Teresa Vogl<sup>1</sup>, and Jonas Witthuhn<sup>1,\*</sup>

<sup>1</sup>Leipzig Institute for Meteorology (LIM), University of Leipzig, Leipzig, Germany

\*These authors contributed equally to this work.

**Correspondence:** heike.kalesse-los@uni-leipzig.de

**Abstract.** Combined continuous long-term ground-based remote-sensing observations with vertically pointing cloud radar and ceilometer are well-suited to identify precipitation evaporation fall streaks (so-called virga). Here we introduce the functionality and workflow of a new open-source tool, the *Virga-Sniffer*, which was developed within the frame of RV *Meteor* observations during the Elucidating the Role of Cloud–Circulation Coupling in ClimAte (EUREC<sup>4</sup>A) field experiment in Jan–Feb 2020 in the Tropical Western Atlantic. The *Virga-Sniffer* Python package is highly modular and configurable and can be applied to multilayer cloud situations. In the simplest approach, it detects virga from time-height fields of cloud radar reflectivity and time series of ceilometer cloud base height. In addition, optional parameters like lifting condensation level, a surface rain flag as well as time-height fields of cloud radar mean Doppler velocity can be added to refine virga event identifications. The netcdf-output files consist of Boolean flags of virga- and cloud detection, as well as base- and top heights and depth for the detected clouds and virga. The sensitivity of the *Virga-Sniffer* results to different settings is explored (in an Appendix). The performance of the *Virga-Sniffer* was assessed by comparing its results to the Cloudnet target classification resulting from using the Cloudnet processing chain. 86 % of the pixel identified as virga correspond to Cloudnet target classifications of precipitation. The remaining 14 % of virga pixel correspond to Cloudnet target classifications of aerosols and insects (about 10 %), cloud droplets (about 2 %), or clear-sky (2 %). Some discrepancies of the virga identification and the Cloudnet target classification can be attributed to applied temporal smoothing. Additionally, it was found that Cloudnet mostly classified "aerosols and insects" at virga edges, which points to a misclassification caused by Cloudnet internal thresholds. For the RV *Meteor* observations in the downstream winter trades during EUREC<sup>4</sup>A, about 42 % of all detected clouds with bases below the trade inversion were found to produce precipitation that fully evaporates before reaching the ground. 56 % of the detected virga originated from trade wind cumuli. Virga with depths less than 0.2 km most frequently occurred from shallow clouds with depths less than 0.5 km, while virga depths larger than 1 km were mainly associated with clouds of larger depths, ranging between 0.5 and 1 km. The presented results substantiate the importance of complete low-level precipitation evaporation in the downstream winter trades. Possible applications of the *Virga-Sniffer* within the frame of EUREC<sup>4</sup>A include detailed studies of precipitation evaporation with a focus on cold pools or cloud organization, or distinguishing moist processes based on water vapour isotopic observations. However, we envision extended use of the *Virga-Sniffer* for other cloud regimes or scientific foci as well.

## 1 Introduction

Trade wind cumuli are the dominant cloud type in the subtropical Atlantic. They typically occur in the form of shallow cumulus humilis or deeper cumulus with a cloud base located near the lifting condensation level (LCL) below 1 km. Trade wind cumuli make up about two thirds of the cloud coverage in the subtropical Atlantic. The other third consists of clouds with bases higher than 1 km, mainly stratiform cloud layers or cloud edges near the trade wind inversion at 2–3 km (Nuijens et al., 2014, 2015). As suggested in Vial et al. (2019), we decided to follow the cloud classification nomenclature of the broader trade cumulus community and will call the Stratocumulus Cumulogenitus class of the world meteorological organization (WMO) cloud atlas "stratiform cloud layers". Precipitation in these clouds mainly forms at temperatures greater than the freezing point by collision and coalescence among droplets formed on the numerous and small cloud condensation nuclei (Reiche and Lasher-Trapp, 2010). Therefore, precipitation generally occurs as light rain/drizzle from stratiform cloud layers or as showers from well-developed trade wind cumuli (Austin et al., 1995; Baker, 1993). The drop size distribution (DSD) of precipitation is modified by a variety of microphysical processes like coalescence or break up of drops as they fall through unsaturated air (Xie et al., 2016). However, evaporation is the only warm subcloud microphysical process that changes the overall amount of liquid water and includes a phase change (Tridon et al., 2017). Precipitation underneath a cloud base is often visible as fall streaks. If the precipitation fully evaporates before reaching the ground, these fall streaks are called virga. Evaporation strength and the resulting cooling rate of air primarily depend on the DSD of the precipitation and on the relative humidity (RH) of the environment. Large droplets evaporate slower than small droplets; at the same time, high relative humidities in the subcloud environment result in slower evaporation, whereas low relative humidities accelerate it (e.g. Xie et al., 2016; Tridon et al., 2017).

While both - full subcloud evaporation of precipitation resulting in virga and partial precipitation evaporation in which rain still reaches the ground - are important, the focus of this manuscript is to introduce a tool that allows for identification of virga. Besides the need to distinguish partial vs. full evaporation due to their different implications for the biosphere, the tool could be used to evaluate satellite-based rain statistics which suffer from blind-zone effects in the near-surface region leading to biases in total precipitation estimates as e.g. shown by Valdivia et al. (2022). However, also for ground-based radar observations, overestimations of surface rain rate retrievals result when evaporation effects are neglected (Rosenfeld and Mintz, 1988; Li and Srivastava, 2001). Case studies of radar-based precipitation evaporation have been performed using observations with sophisticated Micro Rain Radar (MMR) and polarimetric X-band radar (Xie et al., 2016) or dual-frequency Doppler radar spectra (Tridon et al., 2017). Here, we aim to make use of widely available long-term single-frequency vertically-pointing millimetre Doppler cloud radar observations in combination with ceilometer measurements.

Partial and total precipitation evaporation contribute to the moisture and heat budgets of clouds themselves (Emanuel et al., 1994) but also influence the subcloud environment, e.g. due to the formation of cold pools typically caused by precipitation evaporation underneath convective clouds (Langhans and Romps, 2015). Schlemmer and Hohenegger (2014) also found that cold pools resulting from the evaporation of precipitation lead to an increase of the degree of organization of convection, meaning the aggregation of clouds into larger clusters. The strength of low level precipitation evaporation and the resulting

60 evaporative cooling causes differences in cold pool strength and size, which has an effect on the evolution of the convection  
(Dawson et al., 2010). This shows that, on the one hand, precipitation evaporation is important for the organization and re-  
generation of cloud fields via cold pools, but on the other hand, this organization of cloud fields is important for precipitation  
formation. This close connection results in an impact of precipitation evaporation on the radiation budget, as well as moisture  
and heat fluxes (Snodgrass et al., 2009). Summarizing, these studies highlight the need to detect the strength of precipitation  
65 evaporation below convective clouds reliably.

The numerous research efforts made to further understand trade wind clouds, precipitation formation within them and the  
connection to cloud microphysics as well as cloud organization culminated in the field campaign for EUcidating the RoLE  
of Cloud–Circulation Coupling in ClimAte (EUREC<sup>4</sup>A, (Bony et al., 2017; Stevens et al., 2021)). EUREC<sup>4</sup>A was „the most  
ambitious effort ever to quantify how cloud properties co-vary with their atmospheric and oceanic environment across an  
70 enormous (mm to Mm) range of scales“ (Stevens et al., 2021). The campaign consisted of about five weeks of measurements  
in the winter (dry season) trades of the Tropical North Atlantic upstream of Barbados in January and February 2020. It included  
observations of cloud microphysics, cloud-circulation interactions, air-sea interaction, ocean sub-mesoscale processes, and  
ocean mesoscale eddies (Stevens et al., 2021). Airborne measurements were carried out by four research aeroplanes, 2600  
75 drifters, five sail drones and four research vessels. In this study, ground-based remote-sensing observations performed onboard  
the research vessel (RV) *Meteor* operating about 200 km upwind of Barbados between 12.5 and 14.5 °N along the 57.25° W  
meridian are utilized to detect and characterize virga.

The structure of the manuscript is as follows: The relevant instrumentation and data sets for detection of clouds, precipitation  
and virga including the Cloudnet target classification are described briefly in Sect. 2. The *Virga-Sniffer* tool developed in this  
80 study is introduced in Sect. 3. To validate the tool, *Virga-Sniffer* results are compared to the Cloudnet target classification in  
Sect. 4. This section also presents statistical results of detected virga from clouds below the trade inversion height in context  
with cloud macrophysical properties for the entire EUREC<sup>4</sup>A RV *Meteor* observations (18 January to 19 February 2020).  
Sect. 5 comprises a summary, conclusions, and an outlook.

## 2 Data sets

85 For the development of the *Virga-Sniffer*, ground-based remote-sensing observations from a Doppler cloud radar and a ceilome-  
ter operated onboard RV *Meteor* during EUREC<sup>4</sup>A for the period from 18 January to 19 February 2020 were utilized. In  
the following, the used instrumentation and data sets, which are publicly available on the EUREC<sup>4</sup>A AERIS portal (<https://observations.ipsl.fr/aeris/eurec4a/>, last access: 12 August 2022), are briefly described. A summary of instrument specifica-  
tions is given in Table 1. The Cloudnet processing chain is also briefly presented. As additional data, observations from the  
90 onboard RV *Meteor* weather station operated by the German Meteorological Service (DWD) that provided continuous obser-  
vations of standard meteorological parameters such as pressure, temperature, relative humidity, dewpoint temperature, and

precipitation were used, e.g. for flagging times when rain was observed at ground and to determine the lifting condensation level (LCL).

## 2.1 Doppler cloud radar LIMRAD94

95 The Doppler cloud radar that was installed onboard RV *Meteor* is a bi-static frequency-modulated continuous wave (FMCW) radar-radiometer system of type RPG-FMCW-94-DP operating actively in the W-band (94 GHz) and containing a passive radiometer channel at 89 GHz (Küchler et al., 2017). The cloud radar was operated by the Leipzig Institute for Meteorology (LIM) of the University of Leipzig, the instrument is named "LIMRAD94" in the following. While it had previously been used for long-term high-resolution cloud-profiling observations on land (Vogl et al., 2022; Schimmel et al., 2022), EUREC<sup>4</sup>A was  
100 the first ship-deployment of LIMRAD94. To avoid sea-spray accumulating on the cloud radar antenna radomes, the radar was placed on the navigation deck of the ship at 15.8 m above sea level, 4.1 m in the starboard direction and 11 m from the centre of the ship towards the stern.

The two radar chirp program settings, respectively used from 17–29 January 2020 and 31 January 2020 onwards, are shown in Table 2. Due to tests and maintenance, no cloud radar data is available for Jan 30, 2020. The vertical range covered by the  
105 cloud radar observations using the two different chirp table settings was 300–15000 m and 300–13000 m, respectively. Vertical range-gate spacing was between 22–42 m, the temporal resolution amounted to 2.9 s and 1.6 s, respectively. More details on the different chirp sequence settings are given in Table 2.

To exclude the effect of horizontal wind on the observed radar Doppler velocities, the radar needs to point to zenith. To assure that, the instrument was operated within a novel two-axle cardanic mount stabilization designed and manufactured by  
110 Radiometer Physics GmbH, Meckenheim, Germany that allowed for "free-swinging" of the radar to compensate for ship roll- and pitch angles of up to  $\pm 20^\circ$ . An illustration of the radar set-up with cardanic mount is given in Figure 1. Continuous attitude angle measurements by radar built-in motion sensors sampling at 0.5 Hz with an accuracy of  $0.02^\circ$  showed that absolute values of roll and pitch angles experienced by the radar generally were less than  $0.36 \pm 0.31^\circ$  (mean  $\pm$  standard deviation). These small attitude angles do not affect the virga detection performance. A detailed description of the performance of the radar  
115 stabilization platform is beyond the scope of this paper and will be discussed in a separate manuscript.

As a post-processing step to correct for vertical heave of the vessel, a heave correction as described in Acquistapace et al. (2022) was applied to the cloud radar data. Note, that contrarily to Acquistapace et al. (2022), the heave correction was directly applied to the full Doppler spectrum of the W-band radar, instead of to the mean Doppler velocity. Further radar data processing included signal clutter filtering as well as Doppler spectra dealiasing using the pyLARDA software (Bühl et al., 2021a).

## 120 2.2 Ceilometer

Profiles of attenuated backscatter coefficient at a wavelength of 1064 nm are obtained with a ceilometer type Jenoptik CHM15kx. From these profiles, cloud bases were determined using the internal ceilometer cloud base detection algorithm. The ceilometer observations had a range resolution of 15 m and a time resolution of 30 s. It was operated by the Max Planck Institute (MPI) for Meteorology, Hamburg, Germany. For the CHM179158 ceilometer, deployed onboard RV *Meteor* at 20 m above sea level, the

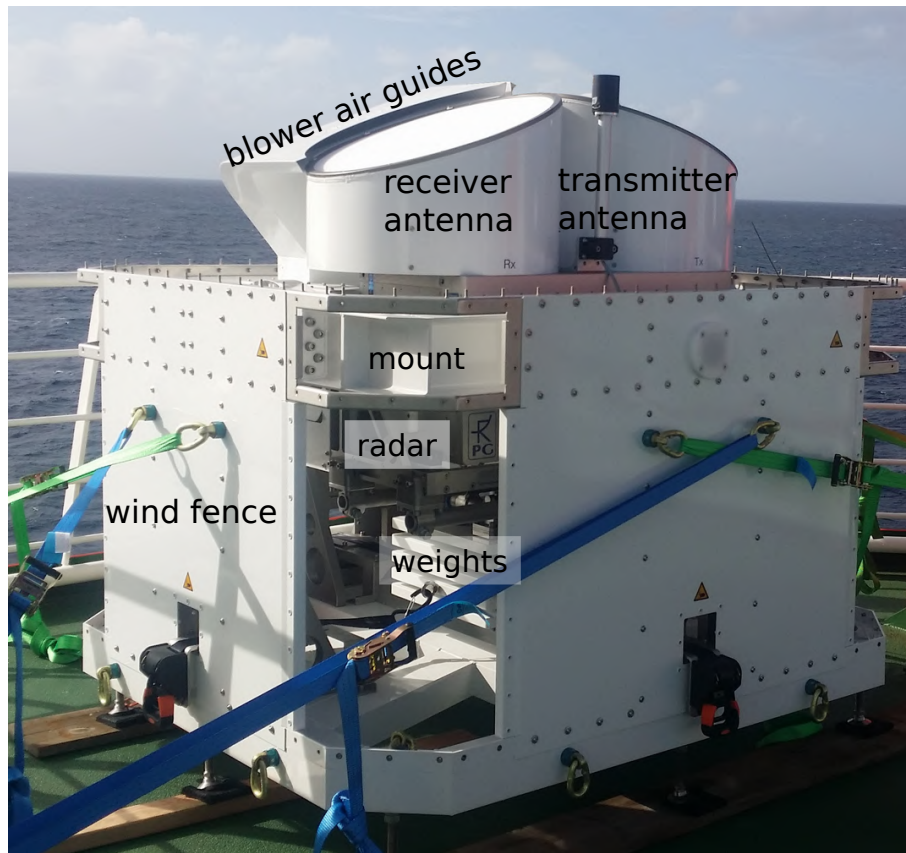


**Figure 1.** 94 GHz FMCW cloud radar "LIMRAD94" inside the cardanic mount. Specific parts of the radar and the cardanic mount are labelled. Photo taken by H. Kalesse-Los.

125 normalization factor (so-called TBC value) was 0.496633. In order to obtain the attenuated backscatter coefficient an additional factor of  $3.2e-12$  is needed, resulting in an overall ceilometer calibration factor of  $1.5892256e-12$  (personal communication with F. Jansen, MPI for Meteorology, Hamburg), which is prescribed during Cloudnet processing (see Sect. 2.4) via a metadata dictionary.

### 2.3 Microwave radiometer LIMHAT

130 Column-integrated values of liquid water path (LWP) were retrieved with a microwave radiometer (MWR) type RPG-HATPRO Generation 5 that was placed in the vicinity of the cloud radar on the navigation deck of the RV *Meteor*. The passive instrument measures brightness temperatures over a range of different frequencies at the centre and slopes of the atmospheric water vapour absorption line (22.23–31.4 GHz) and the oxygen absorption complex (51.26–58.0 GHz). To retrieve LWP from the measured brightness temperatures, statistical algorithms were used by means of a multilinear regression between modelled brightness

**Table 1.** Specifications of instruments and measured/retrieved quantities. For LIMRAD94, in the last three columns the upper values refer to the first chirp table used, the lower values refer to the second chirp table (see Table 2). The values in the last three rows refer to all the measured/retrieved quantities of the respective data source.

Data Source	Frequency $f$ Wavelength $\lambda$	Measured / retrieved quantities	temporal resolution	vertical range	vertical resolution
LIMRAD94	$f = 94$ GHz	Spectral power ( $S_n(v)$ ),			
		Equivalent reflectivity ( $Z_e$ ),	2.93 s	300–15000 m	22.4–29.8 m
		Mean Doppler velocity ( $V_m$ ), Spectrum width ( $SW$ )	1.59 s	300–13000 m	22.4–42.1 m
LIMHAT	$f_1 = 22.23$ – $31.4$ GHz , $f_2 = 51.0$ – $58.0$ GHz	Brightness temperature, Liquid water path (LWP)	1 s		column integral
Ceilometer	$\lambda = 1064$ nm	Attenuated backscatter coefficient, Cloud base height (CBH)	30 s	15–15000 m	15 m

135 temperatures and atmospheric profiles (Löhnert and Crewell, 2003). The retrieval algorithms are based on a radiosonde data set gathered in the subtropical Atlantic (Barbados).

## 2.4 Cloudnet target classification

The Cloudnet processing scheme (Illingworth et al., 2007) combines ground-based remote sensing observations from cloud radar, backscatter lidar (e.g. ceilometer) and microwave radiometer with additional information from a numerical weather pre-  
140 diction model to yield a variety of Cloudnet products, which describe the cloud properties in the vertical column above the observation site. One of these products is the Cloudnet target classification, which indicates which parts of the atmosphere above the site contain ice, liquid, aerosol, insects, etc. Here, we are using the Cloudnet target classification classes for consistency checks of the virga detection method.

To obtain the Cloudnet target classification mask, we applied code from the CloudnetPy package (version 1.33.0, Tukiainen  
145 et al., 2020), i.e. a Python package implementing the Cloudnet processing scheme, to the ground-based remote-sensing observations obtained during EUREC<sup>4</sup>A onboard the RV *Meteor*. With respect to the original Cloudnet software written in Matlab and C, several updates have been made in the Python version, including e.g. improvements in the detection of the melting layer, of liquid layers and of insects that still need to be evaluated. CloudnetPy is an open source project which is being actively developed by a growing community of users. For these reasons, the Python version of the code was chosen instead of the original  
150 (proprietary) Matlab/C implementation of the Cloudnet processing scheme.

For the LIMRAD94 cloud radar, filtering of the data was performed to exclude periods when the chosen radar settings are not supported by CloudnetPy and would lead to erroneous results. Data is filtered at the complete days of 27, 29, 30 and 31 January 2020. During these days, frequent switching between chirp programs are performed for testing. Hourly profiles of pressure,

**Table 2.** Specifications and program settings for LIMRAD94. Two main chirp tables with slightly different settings were used during the campaign. The upper row denotes the first chirp table operated from 17 to 29 January 2020 18:00 UTC, the second row refers to the second chirp table operated from 31 January 2020 22:28 UTC to 29 February 2020 (here data until 19 February 2020 obtained in the EUREC<sup>4</sup>A region of interest was used).

Attributes	Chirp Sequence 1	Chirp Sequence 2	Chirp Sequence 3
Integration time [s]	1.022	0.947	0.966
	0.563	0.573	0.453
Range interval [m]	300–3600	3600–8000	8000–15000
	300–3000	3000–6200	6200–13000
Range vertical resolution [m]	22.4	25.6	29.8
	22.4	37.7	42.1
Nyquist velocity [ $\text{m s}^{-1}$ ]	6.4	5.2	2.9
	7.3	6.1	4.5
Doppler velocity resolution [ $\text{m s}^{-1}$ ]	0.050	0.081	0.089
	0.057	0.095	0.070
Doppler velocity bins	256	128	64
	256	128	128

temperature, and relative humidity from the European Centre for Medium-Range Weather Forecasts Integrated Forecasting System (ECMWF-IFS) complemented the input to CloudnetPy.

### 3 Methodology - Description of the *Virga-Sniffer*

The *Virga-Sniffer* is a profile-based detection scheme for virga events. It is a self-developed Python package (Witthuhn et al., 2022). The detection is based on a set of empirical thresholds, which are manually tuned on the EUREC<sup>4</sup>A data set (Sect. 2) and summarized with their default values in Appendix A. This package provides a tool for detecting precipitation, virga and clouds from profile-by-profile observations of vertically-pointing cloud radar reflectivity and ceilometer observations of cloud base height (CBH), taking into account multilayer cloud situations. The radar data serve as a basis, as they define the temporal and vertical resolution for the *Virga-Sniffer*, which in the case of the EUREC<sup>4</sup>A data set is 1.6–2.9 s and 22–42 m, respectively (see Sect. 2.1). The main result are Boolean masks, which mark clouds, virga and/or precipitation on the radar coordinates (range-gates and time-steps). It is highly configurable, modular and therefore usable for different measurement setups. In addition, virga detection can be refined by additionally considering radar mean Doppler velocity, LCL, and surface rain detection. Example cases presented in the following are based on the default settings of the *Virga-Sniffer* to process the EUREC<sup>4</sup>A data set.

The workflow of the virga detection is separated into three parts, as summarized in Fig. 2:

1. Preprocessing of CBH
- 170 2. Precipitation and cloud detection
3. Virga detection
  - (a) Masking rain events
  - (b) (Optional) virga mask refinement

Note, all modules of the virga mask refinement are entirely optional (step 3b). In order to separate rain and virga events (step 3a)  
175 the *mask\_rain\_ze* module is used, which is based on the radar reflectivity values in the lowest range-gate. Potentially, the *Virga-Sniffer* can be used to mask both rain reaching the surface and virga by opting out of using the rain masks *mask\_rain\_ze* and *mask\_rain*.

### 3.1 Cloud base pre-processing

The ceilometer provides the input values of the CBH. The CBH is a data product of the internal ceilometer processing. For  
180 multilayer cloud situations, multiple CBH are being output, until the ceilometer signal is fully attenuated. Thus, depending on the type of ceilometer and the underlying internal CBH determination algorithm, multilayer cloud situations can also be taken into account. In the *Virga-Sniffer*, cloud layers within a processing interval are sorted, which depends on the given input data (here daily data). Clouds are assigned to specific cloud layers within the processing interval. A cloud layer is identified ~~in the~~  
~~*Virga-Sniffer* by its CBH~~ by the mean CBH of individual clouds assigned to it, which on average differs from other layers over  
185 the processing interval by more than the set threshold of 500 m (*cbh\_layer\_thres*, see Appendix A). The term *layer* is used, if a variable is tied to a specific cloud layer, as the term CBH layer refers to the cloud base height of one cloud layer.

The CBH input data from the ceilometer must be pre-processed to achieve a sorted CBH layer data set before it can be used for virga and cloud detection (see Fig. 2, orange box 1). As the *Virga-Sniffer* is designed to work on the radar data coordinates, the CBH input data, on a temporal resolution of 30 s, is interpolated to the radar time-steps (1.6–2.9 s). Prior to configurable  
190 pre-processing, CBH data is smoothed to avoid outliers in the input data that would complicate pre-processing. For the pre-processing, modular methods are applied to the CBH input data, which can be individually configured. In total, five modules are available. These modules are named *clean & sort*, *split*, *merge*, *add LCL* and *smooth*. Flags and thresholds used to control the modules, and their default values, are summarized in Appendix A.

As default, two iterations of the combination *split*, *merge*, *add LCL* are considered. The module *clean & sort* is applied  
195 in between each step to continuously filter outliers. After these two iterations, a last smoothing step is applied. As a final step, gaps in the processed CBH data smaller than the threshold *cbh\_fill\_limit*, which is one minute by default, are filled by linear interpolation (the filling method can be chosen with the option *cbh\_fill\_method*, see Appendix A). This step to fill gaps in the CBH layers is applied to increase the detection coverage, assuming negligible variability of CBH during a time frame



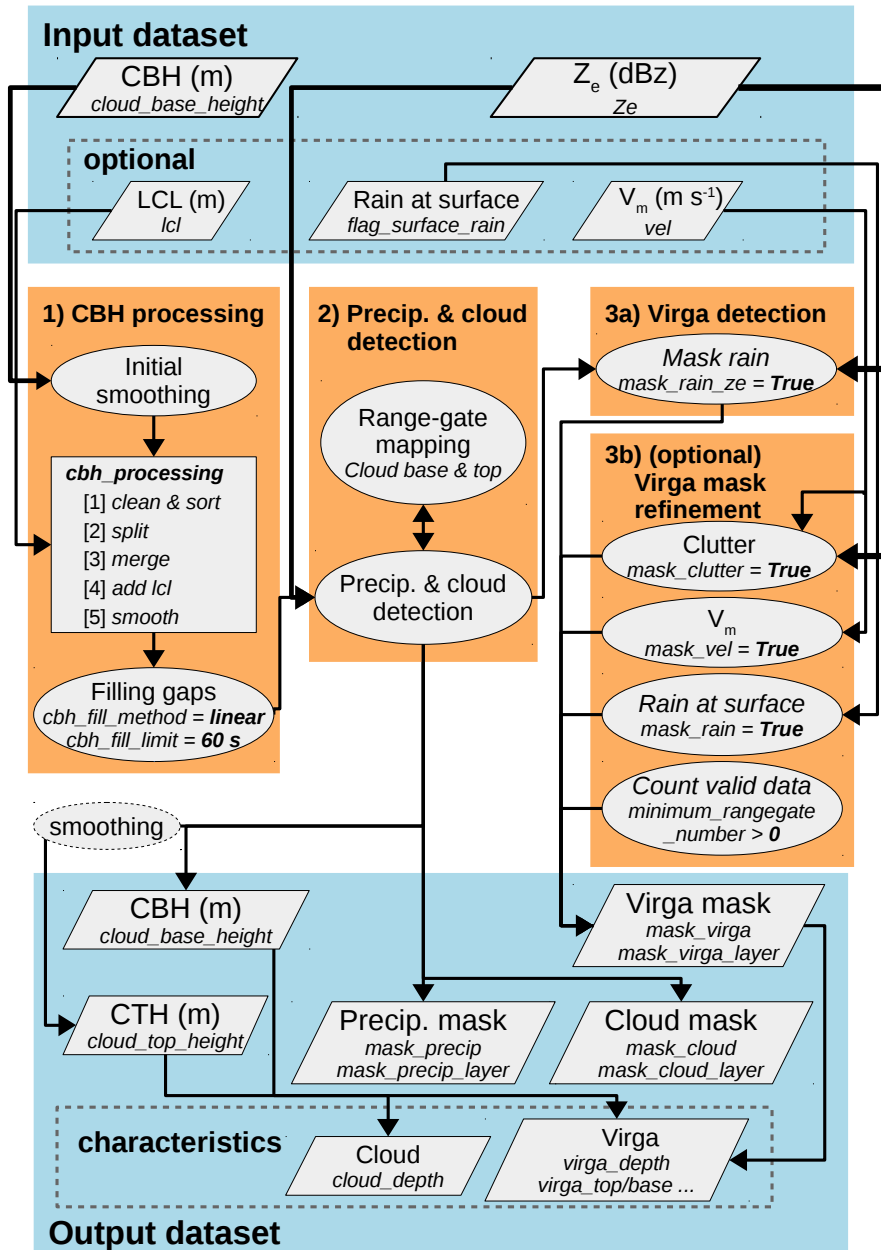


**Figure 2.** The workflow of the *Virga-Sniffer* virga detection. Data sets are shown as polygons, applied methods as ellipses. The submodule *cbh\_processing* is shown as square, listing implemented methods.  $Z_e$  and  $V_m$  refer to the radar variables reflectivity and mean Doppler velocity, respectively. The arrows show the data flow within the *Virga-Sniffer*. The data is processed from the input data set step by step, starting with (1) *CBH processing*, until stored in the output data set. Flags to enable certain virga mask refinements are denoted in italics with their default setting.

controlled by the *cbh\_fill\_limit* threshold. Larger CBH gaps remain, as filling them might lead to non-physical results of CBH  
200 and false positive virga detection.

The individual modules are described below:

1. *clean & sort*: The valid data points of each CBH layer are counted and compared to the number of data points for the total  
205 processing interval. If the number is lower than the given threshold of 5 % by default, the data of this layer is removed  
(*clean*). After the cleaning, the remaining layers are sorted in ascending order by comparing their mean height over the  
processing interval (*sort*).
2. *split*: The CBH data set is iterated successively layer by layer. For each layer, outliers according to given threshold  
settings (by default 500 m above and below the current layer mean) are identified and added to new layers created above  
and below the current layer. This process is re-iterated until no new layers are created.
3. *merge*: Merging CBH layer data by successively iterating all layers and comparing lower layers to all layers above them.  
210 If the distance of the compared layers is smaller than the given threshold setting (by default 500 m above current layer  
mean), upper layer data will be re-assigned to the lower layer, or merged by mean value if both layers hold valid data.
4. *add LCL*: If LCL is provided, it is smoothed by applying a running-median filter of a window size of five minutes by  
default. Then the lowest CBH layer is replaced with the LCL data by default, optionally it can be set to only replace  
nan-values of the lowest CBH layer.
- 215 5. *smooth*: Each layer of the CBH data set is smoothed by applying a running-median filter with a window size of one  
minute.

Note that the *add LCL* module is used here, which utilizes the optional LCL data. With the additional information about the  
LCL, the lowest potential cloud layer can be estimated. This supplements the CBH data of the lowest cloud layer, filling in  
gaps that may occur in the ceilometer data. This ultimately leads to a more complete virga and cloud mask in the *Virga-Sniffer*  
220 output. Nevertheless, the use of the module is optional, since the main CBH information is provided by the ceilometer. To use  
the full potential of the *Virga-Sniffer*, the LCL is included here. The LCL is calculated from surface observations of atmospheric  
pressure, temperature, and humidity from the meteorological observation station on the RV *Meteor* using the method of Romps  
(2017) built into the utilities of the *Virga-Sniffer* package.

### 3.2 Precipitation and cloud detection

225 After the pre-processing of CBH, the radar reflectivity values are used for the initial step of detecting precipitation, clouds and  
cloud top heights (CTH) (see Fig. 2, orange box 2). Figure 3 shows a demonstration example for precipitation, virga and cloud  
detection. A Boolean mask is created, which yields True if the radar reflectivity value is not a nan-value, meaning any kind of  
particles are detected by the radar at the given time and altitude. This mask is successively iterated, starting from each cloud  
base in both up- and downward direction. To do this, the values of the cloud base must be mapped to the radar range-gate

230 resolution. Precipitation events are generally detected downwards from the range-gate containing the measured cloud base, whereas clouds are detected upwards from the next higher range-gate. This step is referred to as range-gate mapping in Fig. 2.

Clouds are detected from iterating the radar reflectivity mask from the cloud base upward, until a gap (nan-value in radar reflectivity) larger than the threshold *cloud\_max\_gap*, of 150 m per default, occurs (see Appendix A and Fig. 3). The CTH value is assigned to the radar range-gate value (top of range-gate) of the last valid radar reflectivity value below the gap. Note, 235 that the detection of clouds is always limited to the area between cloud base and top, meaning virga or precipitation cannot be detected in this range.

Precipitation is detected at each range-gate of the radar reflectivity mask iterating downward from CBH until a gap occurs, which is larger than the threshold *precip\_max\_gap* of 700 m per default (see Appendix A and Fig. 3). This threshold is large by choice, to also capture precipitation which can be observed from tilted fall streaks advected to the radar viewing volume 240 by wind shear. At the same time, the threshold is still small enough to mask out any clutter or a lower cloud layer when the cloud layers are vertically well separated. Since the detection of clouds and precipitation with the *Virga-Sniffer* is carried out for individual profiles and no horizontal linking (in the temporal sense) of these profiles takes place, the handling of tilted fall streaks is one of the most challenging aspects and is realized exclusively by the threshold value of the allowed gap size. The challenges associated with these thresholds (*cloud\_max\_gap* and *precip\_max\_gap*) are discussed in Sect. 3.6. In Appendix B2 245 the sensitivity of the *Virga-Sniffer* results to different settings of these two thresholds is analysed.

A special case occurs, when there are no gaps in radar reflectivity between some cloud base layers, which happens when precipitation originating from a higher cloud falls into a lower layer. In the default setting, the lowest CBH is retained and higher CBH layers are omitted from the processing because no distinction can be made between clouds and precipitation. The lowest CBH in such an event is therefore assigned to initialize precipitation and cloud detection. Note, the handling of this kind 250 of events can be changed to assign the highest cloud base instead, by the configuration flag *cbh\_connect2top* (see Appendix A).

Finally, the detected cloud top values are smoothed as a last step after the processing. The smoothing is applied in the same way as the cloud base by utilizing a rolling median filter of a one-minute window size per default (*cbh\_smooth\_window*). After this processing step, an index mapping of CTH and CBH values to the upper edge of radar range-gate heights is conducted for further processing. This mapping is used to separate the cloud, precipitation and virga masks for the cloud layers respectively, 255 so that the masks can be narrowed down to individual cloud layers.

### 3.3 Virga detection

Until this point, the identification of clouds and precipitation is solely based on the CBH and radar reflectivity (see Fig. 2, orange box 3a). To actually detect virga instead of precipitation that might not fully evaporate in the subcloud layer, the information of surface rain is required. Based solely on CBH and radar reflectivity, this is achieved by testing the lowest range-gate 260 reflectivity value against the threshold *ze\_thres* of 0 dBz per default (see Appendix A). If the radar reflectivity is larger, the precipitation is assumed to reach the surface. These situations are therefore excluded from the virga detection mask.

Virga and cloud detection is sketched in Fig. 3 to demonstrate the usage of thresholds handling gaps in the radar reflectivity signal. The specific cases of Fig. 3 panel (a) are:

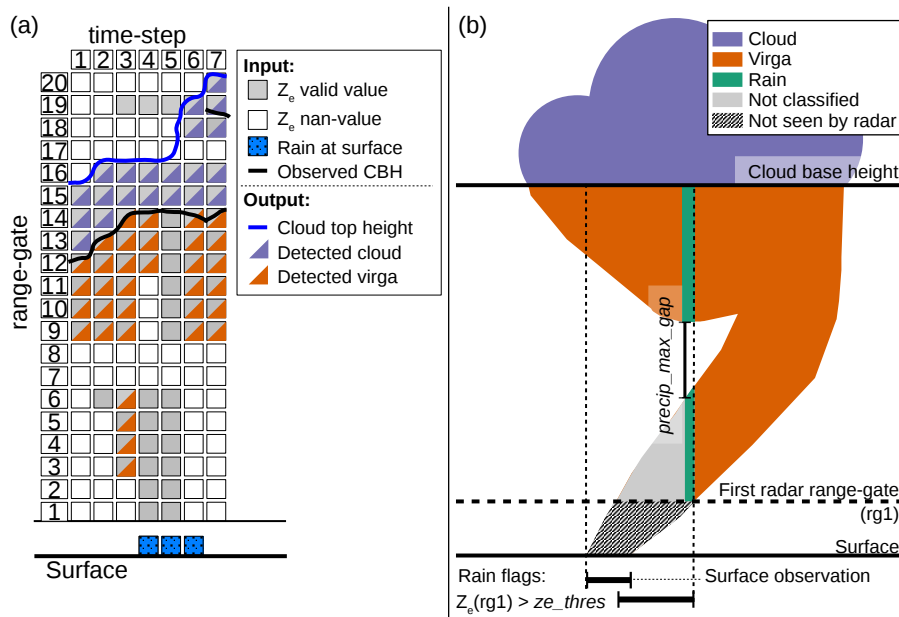


**Figure 3.** Illustration (not to scale) of cloud, precipitation and virga detection from radar reflectivity  $Z_e$ , surface rain flag and cloud base height data, corresponding to step 2 and 3 of Fig 2. In panel (a) the behaviour of the *Virga-Sniffer* in certain situations is shown in detail. Panel (b) shows the benefit and influence of different rain flags, as well as the threshold value of the allowed rain gaps ( $precip\_max\_gap$ ).

265

– *time-step* = 1: The standard case, when precipitation and cloud are detected from the observed CBH. No further considerations have to be made.

– *time-step* = 2: The gap (range-gate (rg) 7–8) is smaller than maximum allowed gap for virga ( $precip\_max\_gap = 700$  m) to count rg 6 as virga, but rg 6 is filtered since the requirement of minimum length of 2 rg is not met, which is a requirement of the virga mask refinement based on the threshold  $minimum\_range\_gate\_number$  (see Sect. 3.4 and Appendix A).

270

– *time-step* = 3: The gap (rg 7–8) is smaller than the threshold, therefore rg 3–6 are counted as virga. In addition, the gap (rg 17–18) is larger than the maximum allowed gap for clouds ( $cloud\_max\_gap = 150$  m) therefore rg 19 is not counted as cloud. In this case, rg 19 could be a cloud, but since the *Virga-Sniffer* detection is tied to the CBH input data, rg 19 cannot be identified. Missing information about the second cloud layer can occur if the ceilometer signal is strongly attenuated by the clouds of the lower layer or by strong precipitation.

275

– *time-step* = 4: The gap (rg 7–11) is larger than the threshold, therefore rg 1–6 are not counted as virga. Therefore, the rain flag at the surface has no effect, as the virga detected in rg 12–14 does not reach the first rg.

– *time-step* = 5: Precipitation is detected from (rg 1–14) as the gap (rg 7–8) is smaller than the threshold. Due to the rain flag at the surface (either by the additional data of surface rain flag, or by exceeding the radar reflectivity threshold in the lowest radar rg,  $ze\_thres = 0$  dBz), no virga is assigned in this profile.

- *time-step* = 6: Same as *time-step* = 5. In addition, the gap (rg 17) is smaller than the maximum allowed gap for clouds, therefore rg 18–19 are counted as cloud. The surface rain flag doesn't lead to a reclassification of the detected virga towards rain, as the first rg has no data.
- *time-step* = 7: Same as *time-step* = 6. In addition, another CBH layer is observed right below rg 19. This CBH layer is not considered, as the gap at rg 17 is smaller than the maximum allowed gap for clouds, and it is not possible to distinguish between clouds and precipitation due to that. Therefore, the lowest CBH is assigned, as in *time-step* = 6 to initialize the detection of clouds and precipitation and the higher CBH is ignored per default (*cbh\_connect2top* = False).

Figure 3 panel (b) demonstrates how rain flags influence the precipitation or virga detection. Since radar observations only provide data starting at a certain height above ground, there may be an offset between the rain flag observed at the surface and the rain flag obtained from the radar signal. In Appendix B3 it is shown how the choice of rain flag affects the virga and cloud detection based on the EUREC<sup>4</sup>A data set. In addition, Fig. 3 panel (b) again shows how the choice of the threshold for the maximum permissible gaps influences the detection of precipitation and the handling of tilted fall streaks.

### 3.4 Virga mask refinement (optional)

Clouds and precipitation detection solely based on radar reflectivity and CBH is refined by using additional data of mean Doppler velocity and surface rain flag (see Fig. 2, orange box 3b).

To mask rain events from the virga detection, the *Virga-Sniffer* provides two methods. The first is based on the radar reflectivity value at the lowest range-gate (here: 300 m) which is compared to the threshold *ze\_thres* of 0 dBz as described in Sect. 3.3. If additional data of surface rain detection is included, this can be incorporated to refine the masking of rain events. In this study, surface rain detection is acquired from the precipitation sensor of the ship's meteorological station.

By using the radar mean Doppler velocity, two additional refinements of the virga mask can be enabled. Firstly, to restrict virga to only falling hydrometeors, each data point is checked against the threshold *vel\_thres* of 0 m s<sup>-1</sup> per default. Data points with positive values of mean Doppler velocity (upward) are omitted from the virga mask (*mask\_vel*, see Fig. A1). Secondly, to mask clutter events, the virga mask is restricted to data points fulfilling the following dependency:

$$V_m > -m * (Z_e/60(\text{dBz})) + c \quad (1)$$

where  $V_m$  and  $Z_e$  denotes the input mean Doppler velocity (m s<sup>-1</sup>) and radar reflectivity factor (dBz), respectively. For convenience,  $Z_e$  is scaled by 60 dBz, as -60 dBz is the minimum valid reflectivity value of LIMRAD94 (for the used radar chirp settings, see Table 2). Slope and intercept of the threshold line are denoted as  $m$  (m s<sup>-1</sup>) and  $c$  (m s<sup>-1</sup>), respectively. A data point is considered virga only if Eq. 1 is fulfilled. With default configuration of *clutter\_m* ( $m = 4$ ) and *clutter\_c* ( $c = -8$ ), unusual combinations of low  $Z_e$  and  $V_m$  are filtered (*mask\_clutter*, see Fig. A1).

In addition to the clutter mask based on the mean Doppler velocity, isolated precipitation events spanning less range-gates than the threshold *minimum\_rangegate\_number* of 2 per default, are excluded. This removes false positive detection due to clutter, which cannot be identified by the combination of high mean Doppler velocity and low radar signal (see Fig. 3, *time-step* = 2).

### 3.5 *Virga-Sniffer* output examples

Example cases of virga detection from RV *Meteor* observations during EUREC<sup>4</sup>A, for which all outlined *Virga-Sniffer* workflow steps were applied, are shown in Fig. 4. The case study examples illustrate the applicability of the *Virga-Sniffer* to different cloud scenarios, such as stratiform cloud layers with virga and a precipitation system (type flower, following the cloud organization pattern naming convention of Stevens et al. (2019)) with virga (Fig. 4 (a) and (b)), stratiform cloud layers producing virga (Fig. 4 (a)–(d)) and virga originating from trade wind cumuli in different development stages (Fig. 4 (a)–(f)) including multi-layer cloud situations.

For easy usability of the *Virga-Sniffer* results, the virga and cloud detection masks are stored in an output data set as Boolean flags with the same dimensions (time, height) as the radar reflectivity input data. In addition, the processed cloud- and virga-base and top heights are stored, as well as some basic characteristics such as cloud depth and virga depth for each profile. When calculating virga depths, the maximum geometric extent is the difference between the initial values of the virga base and top heights. The output variable is called *virga\_depth\_maximum\_extent* and contains the gaps allowed in the detection. Using this value to calculate volumetric features (e.g., LWP) can lead to errors because the liquid water content is then distributed within the gaps that do not physically contain water. Instead, the output variable *virga\_depth* should be used for calculating LWP, as all virga gaps are subtracted in this variable.

### 3.6 Limitations

The virga detection is strongly tuned and manually evaluated for best performance with the EUREC<sup>4</sup>A RV *Meteor* data set (see Sect. 2) and relies on threshold-based tests which might not work in other measurement conditions or different instrumental setups (see Appendix A). Nevertheless, major caveats using this version of the *Virga-Sniffer* are outlined in this section.

Precipitation below CBH, which does not reach the surface, is considered virga. Data points classified as virga are assigned to a certain CBH. In case of a vertical non-continuous radar signal (see Figure 5 at around 03:45 UTC) it is uncertain if the signal originates from a cloud or precipitation. In the case shown in the figure, the signal is unclassified, as the gaps to the cloud base below, at LCL level, are larger than the maximum allowed gap for precipitation. In this situation, there is another cloud layer in an altitude larger than 4 km. In the hypothetical case, these cloud bases were less separated in the vertical, or the maximum gap thresholds were larger, these signals would be classified as virga or cloud by chance, which is potentially false detection. The virga mask refinement using the radar mean Doppler velocity helps to mitigate false detection of clouds and precipitation. Anyway, this caveat can be circumvented completely by not allowing for gaps in virga and clouds which can be achieved by setting the maximum allowed gaps to zero (*precip\_max\_gap* and *cloud\_max\_gap*, see Sect. 3.2 and Appendix A). Doing this would however mean to filter out virga events in strongly-tilted fall streaks or those that are slightly disconnected from the observed cloud base.

If clouds are present in multiple levels, virga detection is challenging, as only the cloud base is known a priori and the vertical extent of the precipitating cloud is not. The *Virga-Sniffer* includes a cloud top detection which is heavily sensitive to the threshold of maximum allowed gaps in the cloud detection. This raises two issues if upper layer clouds are present. First,

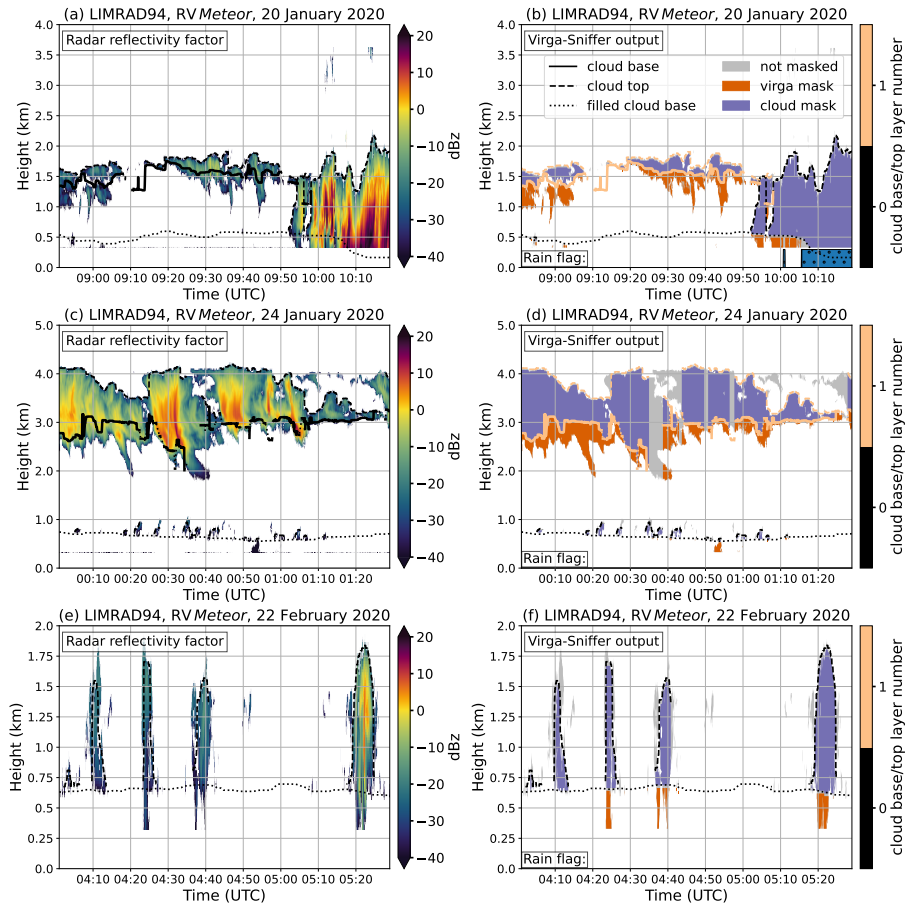


**Figure 4.** LIMRAD94 reflectivity factor  $Z_e$  (panels (a), (c), (e)), and *Virga-Sniffer* output for different cloud situations during EUREC<sup>4</sup>A based on *RV Meteor* observations (panels (b), (d), (f)). The colour bar on the right side panels denotes the maximum number of cloud layers detected during the case study days (count starts at zero for the lowest layer). Panels (a) and (b) show stratiform cloud layers with virga and a warm precipitation system, panels (c) and (d) stratiform cloud layers with virga, and panels (e) and (f) trade wind cumuli with virga. The dotted line labelled "filled cloud base" refers to either LCL values which fill in gaps during the CBH pre-processing or CBH gaps which are filled by interpolation (see Sect. 3.1 and Appendix A).

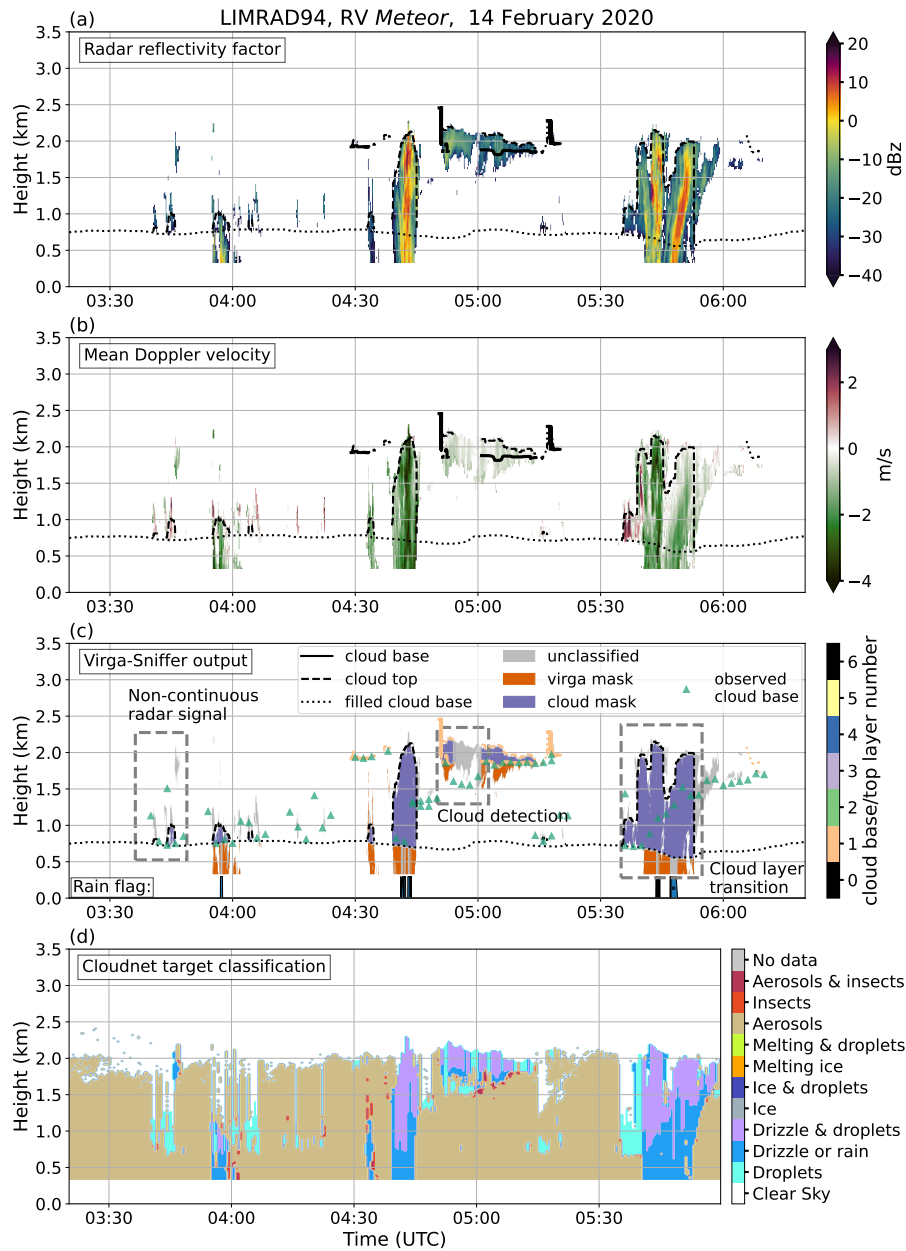


**Figure 5.** (a) LIMRAD94 reflectivity factor, (b) mean Doppler velocity, (c) *Virga-Sniffer* output and (d) Cloudnet target classification for 14 February 2020 as observed from RV *Meteor*. The *Virga-Sniffer* output is marked (dashed boxes) to reveal some caveats which include non-continuous radar signals (03:45 UTC); cloud detection (05:00 UTC); multi layer cloud transition (05:45 UTC). For comparison, the observed CBH from the ceilometer is shown in panel (c). The colour bar denotes the number of cloud layers detected on that day (count starts at zero for the lowest layer).



345 the maximum allowed gap is too small: Due to uncertainties in observational CBH or radar reflectivity data, misalignment of both data or coarse resolution of radar range-gates, ceilometer detected cloud bases might not connect directly to a valid radar signal. Assume the CBH value is below the first range-gate with valid radar signal and the signal gap is larger than the maximum allowed gap (as it is the case in Fig. 5 at around 05:00 UTC): the cloud will not be detected and no cloud top will be assigned. In turn, these range-gates, which are not marked as cloud due to that, could potentially be marked as virga if there was  
350 a higher level cloud with precipitation (this is not the case in Fig. 5). Second, the maximum allowed gap between range-gates with valid radar signal is too large: In this case, clouds will expand over the precipitation from a potential upper layer cloud when they are close to the lower layer cloud top height (not the case in Fig. 5, but illustrated in Fig. 3 time-step 7).

The data points of radar reflectivity might vertically connect through multiple layers of clouds defined by the ceilometer observed CBH. This is the case for example in Fig. 5 at around 05:45 UTC. In this case, the observed cloud base (triangles) is  
355 different from the LCL, but only the LCL is retained in the *Virga-Sniffer* output. During processing with the *Virga-Sniffer*, with the default setting, the cloud bases are assumed to be connected and only the lowest CBH layer is retained. But, the handling of this situation can be changed by the configuration flag *cbh\_connect2top* (see Appendix A). Retaining the highest CBH layer by setting the *cbh\_connect2top* flag to true however raises an issue: The result of the virga mask might show sudden jumps of virga extent, if gaps in layers of cloud base height occur (see also Fig B1). These gaps might occur when the ceilometer beam  
360 is attenuated by the lower level cloud to a large extent. Gaps in ceilometer data can be filled by increasing the layer filling threshold to increase the coverage of upper layer clouds, but might result in false positive detection. In sum, it is challenging to define cloud bases in precipitating clouds, especially if multiple layers of clouds cannot easily be disentangled from the observations. This situation is likely the source of most false positive virga detections. The most conservative option is setting the *cbh\_connect2top* flag to false (default), to mitigate this issue.

365 The limitations identified in this section strongly depend on the input data and atmospheric situation. They can occur at any time. This section is intended to alert potential users of the software of these pitfalls, which may occur to varying degrees in their data set. To be more precise: The issues with "noncontinuous radar signal" and "cloud detection" originate from the facts, that (i) CBH data might be incomplete and (ii) the radar reflectivity might have some gaps if very small cloud droplets are not seen by the radar, which are however detected by the ceilometer. The "cloud layer transition" problem is a bit more tangible. It  
370 does not occur very often when cloud layers in the atmosphere are clearly separable (as it is mostly the case for the EUREC<sup>4</sup>A RV *Meteor* data set). It can become a frequent problem when cloud layers have very large height variations over the course of a measurement period and/or are vertically not well separated.

## 4 *Virga-Sniffer* results from RV *Meteor* observations during EUREC<sup>4</sup>A

### 4.1 Comparison to Cloudnet target classification

375 In order to assess the credibility of the *Virga-Sniffer*, a comparison to the Cloudnet target classification is made for the RV *Meteor* observations during EUREC<sup>4</sup>A. Fig. 6 (inner ring) shows the relative frequency of occurrence of the Cloudnet target classification within virga identified by the *Virga-Sniffer*. The outer ring gives the summarized portions of grouped target

classifications such as liquid only, ice-containing, as well as aerosols and insects. Around 55 % of the hydrometeors within the detected virga are classified by Cloudnet as liquid only, summarizing droplets, drizzle or rain, and the target class drizzle and droplets. Among these targets, only a small fraction (less than 2.5 %) corresponds to droplets, meaning the *Virga-Sniffer* performs well in detecting liquid precipitation. Around 33 % of the pixel identified as virga are among the ice-containing Cloudnet target classes comprised of ice, ice and droplets, melting ice or melting ice and droplets. In total, 86 % of the pixel identified as virga are classified as precipitation by Cloudnet (47.7 % drizzle or rain + 4.9 % drizzle & droplets + 33 % ice). It can thus be concluded, that the *Virga-Sniffer* also performs well in detecting ice precipitation. A small fraction of virga-pixel ( 2 %) are classified as clear sky by Cloudnet. This can be attributed to smoothing of the input radar reflectivity and mean Doppler velocity values at precipitation edges used in the *Virga-Sniffer* algorithm. About 10 % of the virga-pixel are Cloudnet-classified as aerosols and insects.

It is also possible to assess the performance of the *Virga-Sniffer* by only taking into account situations without rain reaching the ground, no rain observed in the lowest radar range-gate and the virga classified by the *Virga-Sniffer*. During these situations the *Virga-Sniffer* misses 15 % of cloud and precipitation related Cloudnet targets (excluding clear sky, aerosols or insects targets). This is mainly due to the determination of the cloud base in the *Virga-Sniffer*. In certain situations, the cloud base used in the *Virga-Sniffer* is lower than the cloud base used in CloudnetPy. As a result, data points in between the cloud bases from CloudnetPy and the *Virga-Sniffer* are identified as the drizzle or rain Cloudnet class, but as cloud by the *Virga-Sniffer*. These situations include: (i) When precipitation connects multi layers of clouds, where the *Virga-Sniffer* retains the lowest CBH only (see Sect. 3.2); (ii) The LCL, which is usually lower than the observed CBH, replaces the lowest CBH layer of the *Virga-Sniffer* (see Sect. 3.1).

As illustrated in the height-resolved overview of the frequency of occurrence of Cloudnet target classification results within virga in Figure 7, aerosols and insects detected within virga mostly occurred within the lowermost 2 km and at virga edges (see Fig. 5 panel (d)). This unexpected Cloudnet insect classification near virga edges is likely caused by strong evaporation leading to radar reflectivity values falling below a threshold value which will be investigated by us in the near future. This effect was observed on many different days during the field experiment. Figure 7 also shows that the liquid-only group of Cloudnet targets occurs mostly below 3 km, while the ice-containing class was mostly detected above 5 km. The separation of the Cloudnet liquid and ice classes is thus according to the mean freezing level at 4.8 km determined from radiosonde data. The majority of ice-containing targets between 4 km and 10 km were observed between 14 February and 16 February 2020. Those days featured continuous and deep cirrostratus and alto stratus.

## 4.2 Virga Properties

The statistics in Table 3 and the subsequent plots were created using output of the *Virga-Sniffer*. The results show the importance of subcloud precipitation evaporation in the winter trades of the tropical Western Atlantic. In the following analysis, only clouds with bases below 4 km, i.e. below the trade inversion height (TIH) are considered. Such clouds were the focus of EUREC<sup>4</sup>A. The relation of virga depth to cloud macrophysical properties, cloud base height and cloud depth is analysed.

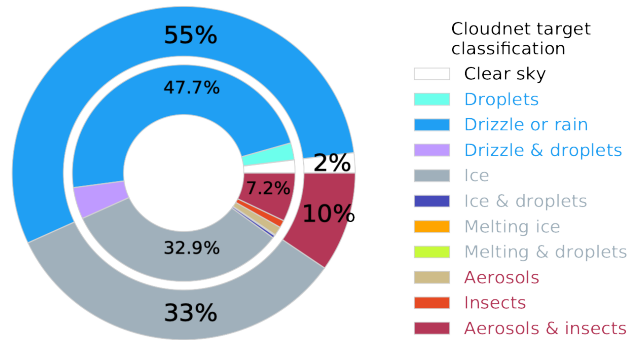


**Figure 6.** Relative frequency of occurrence of the Cloudnet target classification results within virga identified by the *Virga-Sniffer*. The inner ring displays the percentage of the individual Cloudnet target classifications, whereas the outer ring shows the portion of grouped Cloudnet target classes for liquid-only, ice-containing, as well as aerosols and insects indicated by the label color in the legend.

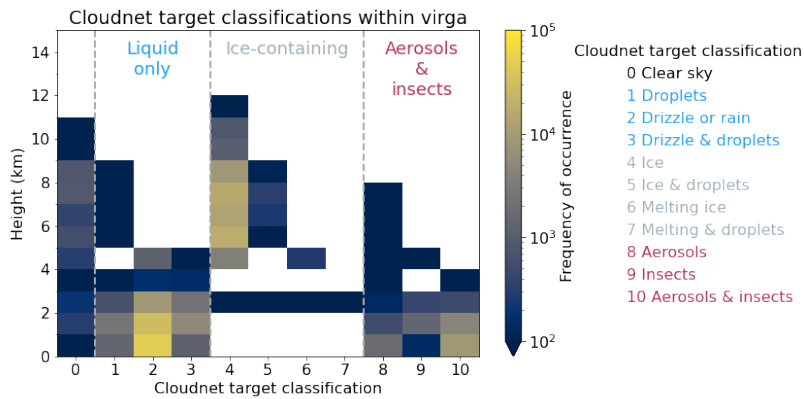


**Figure 7.** Height-resolved frequency of occurrence of the Cloudnet target classification results within virga identified by the *Virga-Sniffer*. The target classes are grouped into three combined target classes: liquid-only, ice-containing, and aerosols and insects.

#### 4.2.1 Virga statistics

About 73 % of all clouds observed on RV *Meteor* during EUREC<sup>4</sup>A had a cloud base below 4 km i.e. below the TIH. Of these 73 %, 56 % produced precipitation that was either detected as virga by the *Virga-Sniffer* or as rain reaching the ground by the WS100-UMB surface rain sensor (see Table 3). These 56 % of precipitating clouds can be subdivided into about 42 % that produced virga, and around 14 % that produced rain reaching the rain sensor onboard the RV *Meteor*. Of all clouds with bases below the trade inversion, 63 % were trade wind cumuli (CBH below 1 km). Approximately 59 % of the trade wind cumuli were precipitating, but only 22 % of all trade wind cumuli produced precipitation that was detected by the DWD rain sensor.

**Table 3.** Precipitation and virga statistics. Precipitation-producing clouds are defined as clouds that either produce virga or rain that reaches the ground. Clouds with their base below 4 km make up about 73 % of the data set. Clouds with ceilometer-detected cloud base below 1 km are classified as trade wind cumuli and considered individually. These clouds make up about 46 % of the entire data set.

Clouds with cloud base below 4 km ...	
... producing precipitation:	56 %
... producing rain reaching the surface:	14 %
... producing virga:	42 %
... .. of which from trade wind cumuli:	56 %
... which are trade wind cumuli:	63 %
Trade wind cumuli ...	
... producing precipitation:	59 %
... producing rain reaching the surface:	22 %
... producing virga:	37 %

The remaining 37 % were cumuli that produced virga. With respect to all detected virga from clouds with bases below TIH, trade wind cumuli made up about 56 %, the remaining 44 % of virga originated from clouds with bases between 1 km and TIH.

#### 420 4.2.2 Virga depth and cloud base height

Figure 8 shows a 2D histogram of virga depth vs. cloud base height. The pronounced cutoff extending from lower left to upper right of the plot is caused by virga reaching the lowest radar range-gate at 0.3 km, since radar-based detected virga depth cannot be larger than CBH minus the lowest radar range-gate height. Numerous virga with varying depths originate from trade wind cumuli which have cloud bases at the LCL between 0.6 and 0.8 km. These virga reach the lowest radar range-gate most frequently and evaporate near the surface. Clouds with bases around 1.5 km and 2.5 km most often produce shallow virga with depths up to 0.2 km. In these heights, mostly stratiform cloud layers are present, reaching up to the base of the trade inversion. From these mostly shallow clouds, shallow virga originate that evaporate before reaching the lowest radar range-gate. However, occasionally virga from these clouds can also reach the lowest radar range-gate, which evaporate before reaching the surface and are thus not detected by the WS100-UMB sensor. This underlines the importance of precipitation evaporation, especially in the lowest 0.3 km of the mostly well-mixed subcloud layer.

#### 4.2.3 Virga depth and cloud depth

Figure 9 illustrates the relation of cloud depth and virga depth. Figure 9 panel (a) shows this relation for clouds with their base below 1 km, respectively the trade wind cumuli. No clear dependency between virga depth and cloud depth can be seen. Large cloud depths combined with small virga depths are likely stronger convective cells (cumulus congestus) with a CBH near the LCL and higher vertical extent. The maximum virga depth the *Virga-Sniffer* can determine is confined by the distance

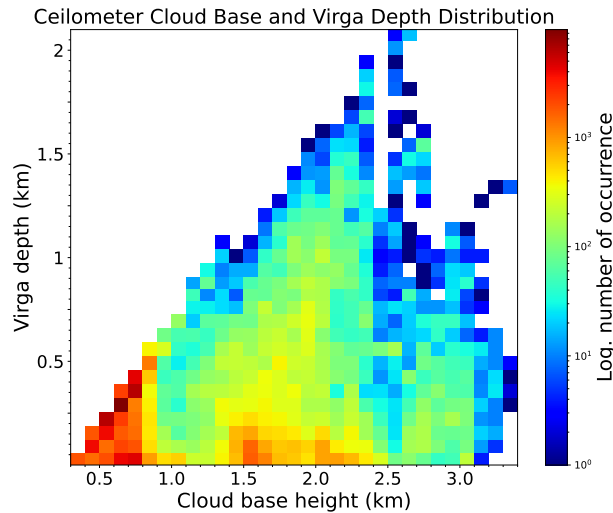


**Figure 8.** 2D histogram of cloud base height and virga depth. The colorbar is logarithmic.

between cloud base and lowest radar range-gate. Thus, virga depth values in (a) are restricted to a few hundred meters. Figure 9 (b) includes only clouds with their base above 1 km and below the TIH. Those are mostly stratiform cloud layers, cloud edges and anvils of convective cells spreading under the trade inversion. Virga depths smaller than 0.3 km often occur from shallow stratiform cloud layers with depths below 0.5 km. For cloud depths between 0.5 and 1 km, the occurrence of virga depths between 0.3 and 1 km is rather evenly distributed. This shows that, inside these boundaries, virga depth is not very dependent on cloud depth. This is also valid for cloud depths between 1 and 1.5 km and virga depths up to 1 km, although these combinations are detected less frequently. Virga depths above 1 km are most frequently produced by clouds with depths between 0.5 and 1 km. Those clouds are the stratiform cloud layers and anvils below the trade inversion, with a cloud base that is high enough to produce deep virga. In a further analysis, the relation of virga depths and liquid water path (LWP) was studied. It is not presented, since no strong dependency of virga depth on column-integrated liquid water path was found.

## 5 Summary, conclusions and outlook

Based on the importance to identify precipitation evaporation reliably, we developed the so-called *Virga-Sniffer*, a new freely-available Python package (Witthuhn et al., 2022). It uses profile-by-profile ground-based remote-sensing observations of ceilometers for cloud base height detection and vertically-pointing Doppler cloud radar to identify clouds and partially or fully evaporating precipitation, and is applicable to multilayer cloud situations. The *Virga-Sniffer* tool is modular and highly configurable, and can thus be applied to different measurement setups.

In this manuscript, the functionality and workflow of the *Virga-Sniffer* tool is explained in detail. It is noteworthy, that while for the most basic approach, only time-height fields of cloud radar reflectivity and time series of cloud base height (CBH) are required, the modular approach of the *Virga-Sniffer* allows for including other optional parameters such as LCL, a surface rain

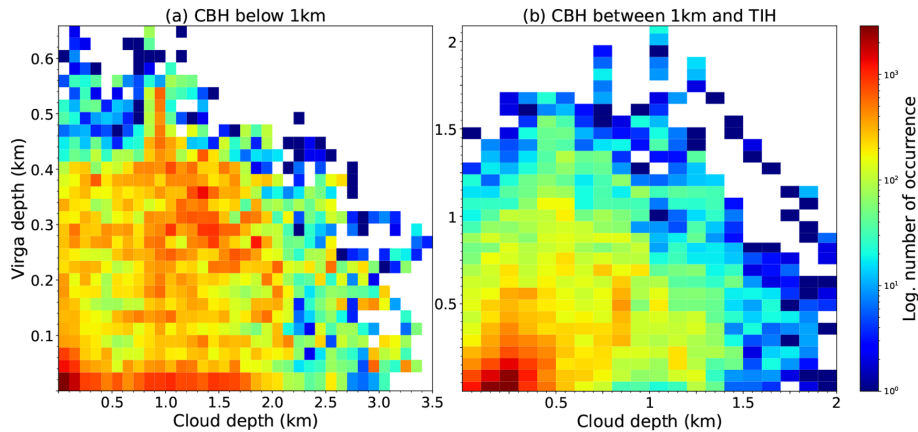


**Figure 9.** 2D Histograms of cloud depth and virga depth. The colorbar is logarithmic. In panel (a) cloud depths and virga depths for clouds with a base below 1 km are shown. Panel (b) shows the same, but for clouds with their base between 1 km and the trade inversion height (TIH).

455 flag, and time-height fields of cloud radar mean Doppler velocity. These additional data makes refinements of the virga event identification possible. The *Virga-Sniffer* output does not only contain the actual Boolean flags of virga and cloud detections in the same time-height grid as the radar input data, but it also provides several virga and cloud properties, including base and top heights as well as depth. In addition, the output contains the flags for the identification of rain reaching the surface. Limitations of the *Virga-Sniffer* are also described. We would like to point out that the virga detection with the *Virga-Sniffer* was developed and optimized for the RV *Meteor* data set obtained during EUREC<sup>4</sup>A. For different instrument setups, cloud types or climate zones, threshold modifications by the *Virga-Sniffer* user are needed to optimize the results.

460

To evaluate the *Virga-Sniffer*, we compared the detected virga events to the Cloudnet target classifications. Summarizing, within all pixel classified as virga by the *Virga-Sniffer*, 86 % were classified by Cloudnet as precipitation (52 % liquid-phase, 34 % ice-phase). The remaining 14 % are either Cloudnet-classified as aerosols and insects (about 10 %), cloud droplets (roughly 2 %), or clear-sky (2 %). We conclude that the performance of the *Virga-Sniffer* compared to the Cloudnet target classification is good. Some discrepancies are expected due to smoothing at precipitation edges as well as ceilometer CBH-smoothing as part of the pre-processing of the *Virga-Sniffer*. The Cloudnet target classification "aerosols and insects" mostly occurred at virga edges and is likely related to Cloudnet thresholds for target classifications, which we will explore further.

465

The *Virga-Sniffer* tool was used for virga identification for the entire RV *Meteor* data set gathered within the frame of EUREC<sup>4</sup>A from 18 January to 19 February 2020. Statistical results showed that 73 % of the observed clouds had bases below 4 km; 63 % of them were trade wind cumuli with a cloud base below 1 km. For the RV *Meteor* data set, 42 % of all clouds below 4 km produced precipitation that fully evaporated before reaching the ground. This marks the importance of strong precipitation evaporation in the downstream winter trade wind zone. With respect to all detected virga from clouds with bases below the TIH, virga from trade wind cumuli make up about 56 %. Trade wind cumuli were found to produce virga of varying

470

475 depths, but a large fraction of these virga tend to reach the lowest radar range-gate in 0.3 km. This means the precipitation evaporates between 0.3 km and ground level and therefore has a strong contribution to near-surface evaporation. Clouds with bases between 1 km and 4 km, which are either stratiform cloud layers or cloud edges of convective cells below the trade inversion, were identified as important virga producers. Stratiform cloud layers with their base around 1.5 km and 2.5 km frequently produce either virga with small depths up to 0.2 km or virga reaching the lowest radar range-gate. This means their  
480 virga can reach depths of over 1.5 km and shows that they also contribute to low level evaporation.

We would like to finish this study with highlighting for which kinds of studies the *Virga-Sniffer* might for example be used in the future. A straightforward application is to use the *Virga-Sniffer* for identifying virga and determining macrophysical properties such as virga depth in relation to cloud base height and cloud depth as they are a pre-requisite for detailed evaporation studies as e.g. done by Xie et al. (2016) and Tridon et al. (2017). Other possible applications of the *Virga-Sniffer*  
485 include enhancing studies of precipitation evaporation in the context of cold pools and cloud organization within the frame of EUREC<sup>4</sup>A as e.g. done by Vogel et al. (2021) and Touzé-Peiffer et al. (2022). Additionally, studying precipitation and virga characteristics coupled with water vapour isotopic measurements, which was also a focus of EUREC<sup>4</sup>A (Bailey et al., 2022), can help to discern the balance of moist processes which set the humidity profiles. As a near-future goal, we would like to apply it to the long-term remote-sensing data set of the Barbados Cloud Observatory (BCO, Stevens et al. (2016)) to contrast  
490 precipitation evaporation in the dry and wet season. While the *Virga-Sniffer* was developed within the context of EUREC<sup>4</sup>A and the shown results here focus on warm clouds, the tool is highly modular and configurable and thus applicable to study precipitation evaporation or sublimation originating from other cloud types such as ice and mixed-phase-clouds and can be used in other geographic settings such as orographic terrain or the Arctic. Our virga identification tool might also help to evaluate satellite-based surface precipitation statistics suffering from blind-zone effects, as indicated by Maahn et al. (2014) and  
495 Valdivia et al. (2022).

## Appendix A: *Virga-Sniffer* recommended configuration

The *Virga-Sniffer* utilizes a variety of flags and thresholds to detect virga from the given input data. The configuration is freely user-configurable via a configuration dictionary, which is merged with the default values. In the following all default values of configuration flags, thresholds and settings are summarized. This default setup is used to process the EUREC<sup>4</sup>A RV *Meteor*  
500 data set described in Sect. 2. A full description of each configuration parameter can be found in the documentation (Witthuhn et al. (2022), <https://virga-sniffer.readthedocs.io>, last access 10 January 2023).

### A1 Flags

Flags are Boolean values which control certain functionalities of the *Virga-Sniffer*:

- *cbh\_connect2top* = False: This flag changes how situations where precipitation falling from the upper into lower CBH  
505 layers are handled. In the default setting (False), the lowest CBH is retained and higher CBH layers are omitted from processing because no distinction can be made between clouds and precipitation from higher layers if there is a contin-

uous radar signal in the profile. Therefore, the default setting is most conservative to avoid false detection of virga. For True, the top CBH layer is retained and the lower CBH layer is omitted from processing. This approach results in more precipitation data points, but it is prone to misclassification of cloud droplets as precipitation.

- 510 – *lcl\_replace\_cbh* = True: When additional LCL data is provided, this flag changes the behaviour of the *add LCL* module for CBH preprocessing (see Sect. 3.1). In the default setting (True), the LCL data completely replaces the lowest ceilometer CBH layer. If False, the LCL data is merged with the lowest ceilometer CBH layer by replacing only missing values.
- *require\_cbh* = True: In the default setting, detected precipitation must always be related to a CBH value. This prevents,  
515 that in case of data gaps in the ceilometer CBH data, a cloud is misclassified as precipitation.
- *mask\_clutter* = True: The virga mask is refined by filtering data which is probably clutter based on Eq. 1.
- *mask\_rain* = True: This configuration uses the ancillary data of the *flag\_surface\_rain* variable from the input data set. Data points which are classified as precipitation are classified as virga if rain is not observed at the surface. This check is applied to the lowest present cloud layer at any given time.
- 520 – *mask\_rain\_ze* = True: Similar to *mask\_rain*, but instead of using *flag\_surface\_rain* from the input data set, the radar reflectivity at the lowest range-gate is tested against the *ze\_thres* threshold in order to distinguish between rain and virga.
- *mask\_vel* = True: The virga mask is refined by filtering data with mean Doppler velocity values larger than *vel\_thres* threshold.

## A2 Thresholds

525 Virga detection specific thresholds:

- *clutter\_c* =  $-8 \text{ m s}^{-1}$ : Intercept of the linear masking dependency (see Eq. 1).
- *clutter\_m* =  $4 \text{ m s}^{-1}$ : Slope of the linear masking dependency (see Eq. 1).
- *cloud\_max\_gap* = 150 m: Assigns the maximum allowed gap for cloud detection.
- *minimum\_rangegate\_number* = 2: In case of non-continuous radar signal in a profile, isolated continuous range-gates  
530 with valid radar signal are used only if the number of range-gates is greater than this threshold.
- *precip\_max\_gap* = 700 m: Assigns the maximum allowed gap for precipitation detection.
- *vel\_thres* =  $0 \text{ m s}^{-1}$ : Threshold for the virga mask refinement based on mean Doppler velocity.
- *ze\_thres* = 0 dBz: If the value of radar reflectivity of the lowest range is larger than *ze\_thres*, precipitation is assumed to reach the ground and not considered as virga in the lowest cloud layer.



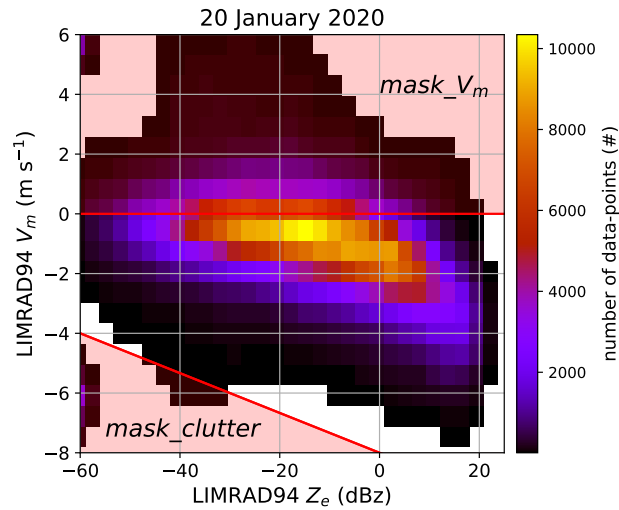


**Figure A1.** Heatmap of the mean Doppler velocity  $V_m$  and radar reflectivity  $Z_e$  during EUREC<sup>4</sup>A from the RV *Meteor* on 20 January 2020. Demonstration of masking based on  $V_m$  data. Data points from red shaded regions are not considered as virga. The velocity mask ( $mask_{V_m}$ ) restricts virga events to falling hydrometeors. The clutter mask ( $mask_{clutter}$ ) removes non-physical values of high negative  $V_m$  while low radar reflectivity factors are observed, which is probably clutter from the radar observation.

535 Cloud base preprocessing specific thresholds:

- $cbh\_clean\_thres = 0.05$ : Threshold used for cleaning cloud base layers during the preprocessing.
- $cbh\_fill\_limit = 60$  s: Defines the maximum gap within cloud layers to be filled by interpolation method  $cbh\_fill\_method$  (see Sect. 3.1).
- $cbh\_layer\_thres = 500$  m: Threshold used for splitting cloud base layers during the preprocessing.
- 540 –  $cbh\_smooth\_window = 60$  s: Window size for the median-filter smoothing of cloud base height and cloud top values.
- $lcl\_smooth\_window = 300$  s: Window size for median-filter smoothing of the lifting condensation level data.

### A3 Special configuration

Apart from thresholds, the cloud base preprocessing is controlled by specialized configuration:

- $cbh\_fill\_method = slinear$ : This defines the method of filling cloud base gaps smaller than  $cbh\_fill\_limit$ .
- 545 –  $cbh\_processing = [2, 1, 3, 1, 4, 2, 1, 3, 1, 4, 5]$ : This list defines the methods applied for preprocessing (see Fig. 2).

**Table B1.** Effects of different thresholds and settings related to the CBH of the *Virga-Sniffer* on the EUREC<sup>4</sup>A data set. The values shown refer to the deviation (%) of the total number of data points / time-steps which are identified as virga / cloud to the total number of data points / time-steps using the default setting. The total number of data points includes both changes in virga depth and time-steps with virga. Defaults and respective test value of the setting or threshold are indicated in the first and second columns (True = T, False = F).

#	setting	value(s)	virga detection						cloud detection					
			$\Delta$ data-points (%)			$\Delta$ time-steps (%)			$\Delta$ data-points (%)			$\Delta$ time-steps (%)		
			layer: all	1st	2+	all	1st	2+	all	1st	2+	all	1st	2+
1	<b>CBH preprocessing</b>	F, 2, 500, 5	0	0	0	0	0	0	0	0	0	0	0	0
2	<i>require_cbh</i> = T	T, -, 500, 5	77	380	-57	29	169	-48	-6	39	7	45	161	-45
3	<i>cbh_processing</i> = 2*	T, 1, 500, 5	1	0	1	4	0	8	3	0	35	3	-0	12
4	<i>cbh_layer_thres</i> = 500 m	T, 3, 500, 5	-3	-0	-4	-3	-0	-7	-4	-0	-19	-3	0	-9
5	<i>cbh_clean_thres</i> = 5 %	T, 2, 60, 5	-53	-0	-78	-49	0	-83	-37	0	42	-25	20	-58
6	*iterations of [2,1,3,1,4,1] (see Sect. 3.1)	T, 2, 1000, 5	-15	-0	-22	-8	-1	-13	-1	-0	-18	-10	0	-21
7		T, 2, 500, 0	20	0	29	27	1	55	14	0	220	23	1	86

## Appendix B: Sensitivity of *Virga-Sniffer*

The sensitivity of the setting parameters of the *Virga-Sniffer* is evaluated using the EUREC<sup>4</sup>A data set. Table B1 and Table B2 shows the deviation of virga and cloud detection versus the proposed default settings. The deviation is thereby expressed in percentage change of the sum of data points of each column identified as virga or cloud, or number of time-steps when virga or clouds are detected in any range-gate. This shows, if changing a specific setting results in less or more total data points detected as virga / cloud ( $\Delta$  data-points), or in less or more virga / cloud events in time ( $\Delta$  time-steps).

### B1 Cloud base pre-processing

The virga and cloud detection is most sensitive to settings of the CBH pre-processing (Sect. 3.1). This is not surprising, as the identification of clouds and virga is initiated from the input (and then pre-processed) CBH data. The three main configuration settings affecting the CBH processing are *require\_cbh*, *cbh\_processing* and *cbh\_layer\_thres*, whereas *cbh\_processing* and *cbh\_layer\_thres* are strongly depended on the *clean*-module (see Sect. 3.1) controlled by the threshold *cbh\_clean\_thres*.

First, if the configuration flag *require\_cbh* is set to False, a value of CBH is not required to initiate cloud and virga detection, instead, virga detection is initiated from the surface or a lower cloud top upwards. This choice can be useful in single layer cloud situations to capture vertically oriented fall streaks. In multi-layer cloud situations this is prone to error, as upper layer clouds, for which no ceilometer CBH is detected, might be falsely identified as virga. In case of the used EUREC<sup>4</sup>A data set, virga events from higher cloud layers are identified and attributed also in the first layer within gaps in the trade wind cumuli. Thus, virga is identified in significantly more profiles and range-gates in the first layer, but, in total, virga identification is not strongly affected as shown in Table B1, row 1.

Second, when switching off the CBH preprocessing (Table B1, row 2) most virga is connected to the first cloud layer, as  
565 cloud layers are no longer identified, split and sorted by altitude. On the other hand, significantly more virga is detected in  
total (77%), since cloud layers with fewer data are removed during processing (*clean*-module). The total number of data  
points classified as virga reduces progressively when increasing the number of iterations of the standard CBH preprocessing  
procedure, since outliers are isolated and removed with each iteration (row 3 for one iteration and row 4 for three iterations),  
however the effect is minor. The reduction of data points classified as virga, when CBH preprocessing is applied, depends  
570 mainly on how aggressively the cleaning is done in between the processing steps (see Sect. 3.1). For the EUREC<sup>4</sup>A data set,  
*cbh\_clean\_thres* is rather aggressive, with a default value of 5%.

Finally, setting *cbh\_layer\_thres* does not affect the amount of virga and clouds detected. However, if the threshold is de-  
creased, more cloud layers will be detected per observation period, resulting in many of these layers containing few data points  
and therefore being removed by the *clean*-module. Therefore, a decrease in *cbh\_layer\_thres* leads to a reduction in detected  
575 data points (Table B1, row 5). Note, doubling *cbh\_layer\_thres* also reduces the total amount of data points classified as virga  
by 15% (Table B1, row 6). This indicates, that the combination of the default values of *cbh\_layer\_thres* and *cbh\_clean\_thres*  
are chosen in a way to remove outliers but do not affect the detection of clouds and virga on the EUREC<sup>4</sup>A data set. The  
effect of *cbh\_clean\_thres* is demonstrated again in Table B1, row 7 where standard CBH is performed, but clean-up is turned  
off by setting the threshold to zero. The total number of profiles containing virga is similar to the test in which the entire CBH  
580 processing is turned off (row 2).

## B2 Precipitation and cloud detection

The initial precipitation and cloud detection is initialized for each cloud layer at all time-steps (see Sect. 3.2). This detection is  
influenced by the settings of the maximum allowed vertical gaps in the radar reflectivity data. In Table B2, rows 1–8 shows the  
impact of changing these settings by the thresholds *precip\_max\_gap* and *cloud\_max\_gap*.

585 The purpose of *precip\_max\_gap* is to detect also tilted fall streaks far below a cloud base (due to horizontal transport by  
wind shear), and at the same time prevent false detection of clouds as precipitation. The default setting of *precip\_max\_gap*  
is 700 m. Setting *precip\_max\_gap* to zero, which is the safest option to prevent false positive detection, results in about 21%  
less total number of data points for the EUREC<sup>4</sup>A data set (row 1). On the other hand, allowing for infinite large gaps (row 4)  
only adds about 6% of data, as the detection always stops at the lowest range-gate or the lower cloud top, which are detected  
590 first. It can be concluded, that the choice of *precip\_max\_gap* does not impact depth and frequency of occurrence of detected  
precipitation strongly. It is however required to detect tilted fall streaks, which are not connected to the CBH of one profile.

Similarly, the sensitivity to the threshold *cloud\_max\_gap* for cloud detection is analysed. The difference is, that the cloud  
detection happens first and thus sets the lower limit for precipitation detection in each cloud layer, respectively. Thus, if this  
threshold is chosen too large, any precipitation above the first 8 cloud layer will be identified as cloud (row 8). Note, that a  
595 lower value or a value of zero for *cloud\_max\_gap* strongly influences the amount of data points identified as cloud, but does  
not strongly affect precipitation or virga detection (rows 5–6). For virga detection, setting *cloud\_max\_gap* larger than zero is  
useful to prevent false detection of virga at non-identified cloud tops.

**Table B2.** As Table B1, for thresholds and settings for virga and cloud detection and virga mask refinement.

#	setting	value(s)	virga detection						cloud detection					
			$\Delta$ data-points (%)			$\Delta$ time-steps (%)			$\Delta$ data-points (%)			$\Delta$ time-steps (%)		
			layer: all	1st	2+	all	1st	2+	all	1st	2+	all	1st	2+
1		0	-21	-13	-24	-15	-22	-16	0	0	0	0	0	0
2	<b>max. gap in virga</b> (m) <i>precip_max_gap</i> = 700	350	-4	-1	-6	-3	-3	-5	0	0	0	0	0	0
3		1400	2	0	3	2	0	4	0	0	0	0	0	0
4		inf	6	0	8	3	1	7	0	0	0	0	0	0
5		0	9	0	13	2	0	6	-13	-18	-9	-19	-30	-8
6	<b>max. gap in clouds</b> (m) <i>cloud_max_gap</i> = 150	75	6	0	8	1	0	4	-9	-11	-6	-9	-13	-4
7		300	-9	0	-14	-2	0	-7	12	18	7	9	17	1
8		inf	-69	0	-100	-60	0	-100	66	187	102	148	368	-60
9	<b>CBH assigning</b> for connecting precip. <i>cbh_connect2top</i> = F	T	43	-16	69	3	-15	15	-12	-32	-12	-0	-13	11

In multi-layer cloud situations, it may not be possible to separate individual cloud layers from the radar signal if it does not have gaps in the vertical. If this is the case, the *Virga-Sniffer* cannot distinguish between cloud and precipitation. Therefore, only the lower cloud layer is considered in these situations to minimize false detection of precipitation. This is controlled via the *cbh\_connect2top* flag, which is set to False by default. If set to True (Table B2, row 9), considerably more data points (43 %) are classified as virga, and data points classified as clouds are reduced.

### B3 Use of optional data

As summarized in Fig. 2, input data of the LCL, a surface rain flag, and the radar mean Doppler velocity is entirely optional. Here, we assess and discuss the effect of not using this optional data.

LCL data can be provided to supplement the CBH data during preprocessing. This supplementation is useful when clouds are generated by lifting (e.g., trade wind cumuli) to fill in gaps in the observed CBH. Since the CBH data in the *Virga-Sniffer* serve as a starting point for cloud and precipitation detection, this, in conjunction with the *precip\_max\_gap* threshold, enables the detection of tilted fall streaks. The total number of virga data points increases by about 48 % when the LCL is not used, as ceilometer CBH, which are usually higher than the LCL are now used to initiate the detection of precipitation, as shown in Fig. B1.

Using a rain flag based on surface observations can improve the separation of rain reaching the surface and virga events. This is optional, as this flag is in addition to a surface rain estimate based on the radar reflectivity of the lowest range-gate (see Fig. 2). The impact of using both, only one or none of the rain flags is demonstrated in Table B3 rows 3–7. As a default, both

**Table B3.** As Table B1, for thresholds and settings for virga detection and virga mask refinement.

#	setting	value(s)	virga detection						cloud detection					
			$\Delta$ data-points (%)			$\Delta$ time-steps (%)			$\Delta$ data-points (%)			$\Delta$ time-steps (%)		
			layer: all	1st	2+	all	1st	2+	all	1st	2+	all	1st	2+
1	<b>LCL</b>	no LCL	48	120	16	7	19	0	-18	-34	18	25	55	0
2		LCL merged	13	46	-1	7	17	2	-1	-3	9	11	21	5
3	<b>rain masks</b> <i>mask_rain</i> =T <i>mask_rain_ze</i> =T with: <i>ze_thres</i> =0 dBz	T, (F, -)	4	11	0	3	9	0	0	0	0	0	0	0
4		F, (T, -10)	-5	-15	-0	-4	-11	-0	0	0	0	0	0	0
5		F, (T, 0)	2	6	0	2	5	0	0	0	0	0	0	0
6		F, (T, 10)	7	21	1	7	18	0	0	0	0	0	0	0
7		F, (F, -)	10	31	1	11	27	0	0	0	0	0	0	0
8	<b>velocity mask</b> <i>mask_vel</i> =T <i>vel_thres</i> =0 m s <sup>-1</sup>	F, -	7	15	4	26	62	3	0	0	0	0	0	0
9		T, -1.0	-49	-24	-60	-41	-24	-55	0	0	0	0	0	0
10		T, -0.5	-16	-8	-20	-15	-11	-19	0	0	0	0	0	0
11		T, 0.5	3	4	3	4	8	3	0	0	0	0	0	0
12		T, 1.0	4	6	3	6	11	3	0	0	0	0	0	0
13	<b>clutter mask</b> <i>mask_clutter</i> =T <i>min._rg._no.</i> =2	F, 0	3	7	2	19	36	11	0	0	0	0	0	0
14		F, 2	1	3	0	7	22	0	0	0	0	0	0	0
15		T, 0	2	4	2	12	16	11	0	0	0	0	0	0
16		T, 4	-6	-6	-6	-17	-16	-18	0	0	0	0	0	0
17		T, 8	-17	-11	-20	-35	-23	-43	0	0	0	0	0	0

615 rain masks are used. Row 7 shows a 11 % increase of time-steps with "virga" when not using any rain mask. The rain events, which make up these 11 %, are masked by the combination of both the rain mask from surface observation and the rain mask based on the radar reflectivity. If the surface observation is not available, the majority of rain events can be masked using the radar reflectivity data only, as time-steps with virga increase by only 2 % compared to using both rain masks (Table B3, row 5). This shows, that adding surface observed rain masking to the *Virga-Sniffer* does not lead to significant improvements for this data set, if the threshold *ze\_thres* is chosen appropriately. The choice of the threshold *ze\_thres* depends on the height of the lowest radar range-gate of the measurement setup and the calibration of the radar reflectivity, and is therefore strongly dependent on the measurement setup. In case of LIMRAD94 at EUREC<sup>4</sup>A, the lowest range-gate is at about 300 m altitude and the calibration convention is that a cloud at 273 K containing one million 100  $\mu\text{m}$  droplets per cubic metre will have a reflectivity of 0 dBz. Rows 4 and 6 of Table B3 shows the impact of changing *ze\_thres* by  $\pm 10$  dBz for the EUREC<sup>4</sup>A setup. 625 The impact of this *ze\_thres* variation is in the order of -4 % to +7 % number of time-steps, for which virga is detected.

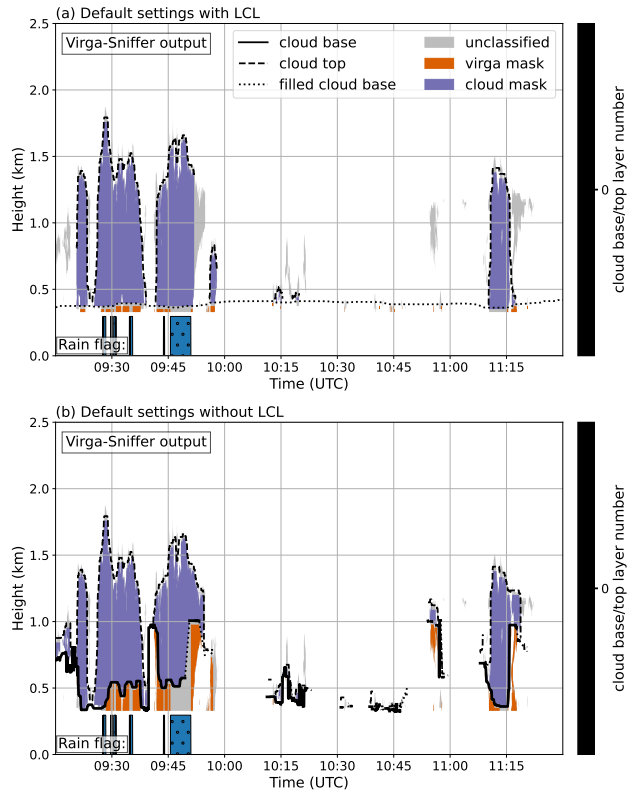


**Figure B1.** *Virga-Sniffer* output from 28 February 2020 with (panel (a)) and without (panel (b)) optional LCL data.

The use of the radar mean Doppler velocity for Virga mask refinement, while optional, can lead to significant improvements. By default, data points with a mean Doppler velocity value greater than the threshold  $vel\_thres$  of  $0 \text{ m s}^{-1}$  are not considered as virga. If this refinement is not used, the total amount of data points increases by 7% (Table B3, row 8), with these additional data points originate primarily from up-drafts below CBH of lower layer cumuli, as evidenced by the substantial 62% increase in virga time-steps in the first cloud layer. These up-drafts are generally stronger than  $1 \text{ m s}^{-1}$ , as an increase from  $vel\_thres$  to  $1 \text{ m s}^{-1}$  (row 12) increases the virga time-steps by 11% only. Further, the radar mean Doppler velocity can be used to mask clutter as shown in Fig. A1. Table B3, row 14 shows the impact of not using the clutter filter. The filter criteria apply to about 1% of detected virga data points and can therefore be considered minor. If the threshold value  $minimum\_range\_gate\_number$  is changed (Table B3, rows 14–17), this leads to proportionately more data points classified as virga if it is reduced, and to fewer data points classified as virga if it is increased. This threshold is useful to prevent misclassification of individual outlier data points, but should not be set too high, otherwise a non-negligible proportion of the data will not be considered.

*Author contributions.* HKL was in charge for the project administration, funding acquisition, shipping, installation, and operation of the instruments of University of Leipzig onboard RV *Meteor* during EUREC<sup>4</sup>A. JR assisted in installation and operation of the instruments and did the data processing. JW, JR and HKL developed the *Virga-Sniffer*. JW performed the *Virga-Sniffer* processing of the EUREC<sup>4</sup>A data. AK used the *Virga-Sniffer* output for analysis of the RV *Meteor* EUREC<sup>4</sup>A data. TV performed the CloudnetPy processing. AF did the comparison to the Cloudnet target classification. All authors contributed to writing and editing the manuscript.

*Competing interests.* The authors declare that they have no competing interests.

*Code and data availability.* The source code of the *Virga-Sniffer* is freely available and hosted on GitHub (Witthuhn et al., 2022). The data measured onboard RV *Meteor* during EUREC<sup>4</sup>A is hosted by the AERIS Portal <https://observations.ipsl.fr/aeris/eurec4a/> (last access: 12 August 2022). This includes data products from the onboard meteorological station operated by DWD, the ceilometer (Jansen, 2020) operated by MPI for Meteorology Hamburg, as well as the Doppler cloud radar LIMRAD94 (Kalesse-Los et al., 2021), and the microwave radiometer LIMHAT (Kalesse-Los et al., 2020) operated by University of Leipzig. Cloudnet processing was done using CloudnetPy (<https://doi.org/10.5281/zenodo.4011843>, (version 1.33.0, Tukiainen et al., 2020)). A setup of pyLARDA (<https://doi.org/10.5281/zenodo.4721311>, Bühl et al. (2021b)) was used for data input and analysis.

*Acknowledgements.* The data used in this publication was gathered in the EUREC<sup>4</sup>A field campaign and is made available through the AERIS portal by data upload through University of Leipzig, MPI for Meteorology Hamburg, and the German Weather Service (DWD). EUREC<sup>4</sup>A is funded with support of the European Research Council (ERC), the Max Planck Society (MPG), the German Research Foundation (DFG), the German Meteorological Service (DWD) and the German Aerospace Center (DLR). We acknowledge the pan-European Aerosol, Clouds and Trace Gases research Infrastructure (ACTRIS) for providing the Cloudnet framework used in this study, which was developed by the Finnish Meteorological Institute (FMI), and is available for download from <https://cloudnet.fmi.fi/>. We also acknowledge ECMWF for providing Integrated Forecasting System (IFS) model data as input for CloudnetPy. Parts of the results in this work make use of the colormaps in the CMasher package (van der Velden, 2020).

The authors would also like to acknowledge the ship crew and Michael Schäfer from University of Leipzig for the excellent support offered in the installation of the equipment on board RV *Meteor*. Thanks also to Alexandros Emmanouilidis who helped a lot in the logistical planning for shipment of the instruments from University of Leipzig to Barbados. Additionally, the authors like to thank Stefan Kinne and Friedhelm Jansen from MPI for Meteorology Hamburg for their support in ceilometer-related questions. Further thanks go to Javier Pasarin Lopez who characterized the cloud radar stabilization platform in his bachelor thesis. Thanks to Claudia Acquistapace for valuable feedback on the *Virga-Sniffer* usability. Finally, we would like to thank the three reviewers (Raphaela Vogel and two anonymous referees) whose comments helped to improve the manuscript.

665 *Financial support.* This research has been supported by the Federal State of Saxony and the European Social Fund (ESF) in the framework of the programme “Projects in the fields of higher education and research” (grant no. 100339509) and ESF-REACT (grant no. 100602743). Further financial support was provided by the German Science Foundation (DFG, grant number FO 1285/2-1).



## References

- Acquistapace, C., Coulter, R., Crewell, S., Garcia-Benadi, A., Gierens, R., Labbri, G., Myagkov, A., Risse, N., and Schween, J. H.:  
670 EUREC<sup>4</sup>A's *Maria S. Merian* ship-based cloud and micro rain radar observations of clouds and precipitation, *Earth System Science Data*, 14, 33–55, <https://doi.org/10.5194/essd-14-33-2022>, 2022.
- Austin, P., Wang, Y., Pincus, R., Kujala, V., et al.: Precipitation in stratocumulus clouds: Observational and modeling results, *Journal of the atmospheric sciences*, 52, 2329–2352, 1995.
- Bailey, A., Aemisegger, F., Villiger, L., Los, S. A., Reverdin, G., Quiñones Meléndez, E., Acquistapace, C., Baranowski, D. B., Böck, T.,  
675 Bony, S., Bordsdorff, T., Coffman, D., de Szoeko, S. P., Diekmann, C. J., Dütsch, M., Ertl, B., Galewsky, J., Henze, D., Makuch, P., Noone, D., Quinn, P. K., Rösch, M., Schneider, A., Schneider, M., Speich, S., Stevens, B., and Thompson, E.: Isotopic measurements in water vapor, precipitation, and seawater during EUREC<sup>4</sup>A, *Earth System Science Data Discussions*, 2022, 1–40, <https://doi.org/10.5194/essd-2022-3>, 2022.
- Baker, M.: Trade cumulus observations, in: *The Representation of Cumulus Convection in Numerical Models*, pp. 29–37, Springer, 1993.
- 680 Bony, S., Stevens, B., Ament, F., Bigorre, S., Chazette, P., Crewell, S., Delanoë, J., Emanuel, K., Farrell, D., Flamant, C., Gross, S., Hirsch, L., Karstensen, J., Mayer, B., Nuijens, L., Ruppert, J. H., Sandu, I., Siebesma, P., Speich, S., Szczap, F., Totems, J., Vogel, R., Wendisch, M., and Wirth, M.: EUREC4A: A Field Campaign to Elucidate the Couplings Between Clouds, Convection and Circulation, *Surveys in Geophysics*, 38, 1529–1568, <https://doi.org/10.1007/s10712-017-9428-0>, 2017.
- Bühl, J., Radenz, M., Schimmel, W., Vogl, T., Röttenbacher, J., and Lochmann, M.: pyLARDA v3.2, <https://doi.org/10.5281/zenodo.4721311>,  
685 2021a.
- Bühl, J., Radenz, M., Schimmel, W., Vogl, T., Röttenbacher, J., and Lochmann, M.: pyLARDA v3.2, <https://doi.org/10.5281/ZENODO.4721311>, 2021b.
- Dawson, D. T., Xue, M., Milbrandt, J. A., and Yau, M.: Comparison of evaporation and cold pool development between single-moment and multimoment bulk microphysics schemes in idealized simulations of tornadic thunderstorms, *Monthly Weather Review*, 138, 1152–1171,  
690 2010.
- Emanuel, K. A., David Neelin, J., and Bretherton, C. S.: On large-scale circulations in convecting atmospheres, *Quarterly Journal of the Royal Meteorological Society*, 120, 1111–1143, 1994.
- Illingworth, A. J., Hogan, R. J., O'Connor, E., Bouniol, D., Brooks, M. E., Delanoë, J., Donovan, D. P., Eastment, J. D., Gaussiat, N., Goddard, J. W. F., Haefelin, M., Baltink, H. K., Krasnov, O. A., Pelon, J., Piriou, J.-M., Protat, A., Russchenberg, H. W. J., Seifert, A., Tompkins,  
695 A. M., van Zadelhoff, G.-J., Vinit, F., Willén, U., Wilson, D. R., and Wrench, C. L.: Cloudnet: Continuous Evaluation of Cloud Profiles in Seven Operational Models Using Ground-Based Observations, *B. Am. Meteorol. Soc.*, 88, 883–898, <https://doi.org/10.1175/BAMS-88-6-883>, 2007.
- Jansen, F.: Ceilometer Measurements RV Meteor, EUREC4A, <https://doi.org/10.25326/53>, medium: NetCDF,ASCII Type: dataset, 2020.
- Kalesse-Los, H., Röttenbacher, J., Schäfer, M., and Emmanouilidis, A.: Microwave Radiometer Measurements RV Meteor, EUREC4A,  
700 <https://doi.org/10.25326/77>, medium: NetCDF Type: dataset, 2020.
- Kalesse-Los, H., Röttenbacher, J., and Schäfer, M.: W-Band Radar Measurements RV Meteor, EUREC4A, <https://doi.org/10.25326/164>, medium: NetCDF Version Number: 1.0 Type: dataset, 2021.

- Küchler, N., Kneifel, S., Löhnert, U., Kollias, P., Czekala, H., and Rose, T.: A W-Band Radar–Radiometer System for Accurate and Continuous Monitoring of Clouds and Precipitation, *Journal of Atmospheric and Oceanic Technology*, 34, 2375–2392, <https://doi.org/10.1175/jtech-d-17-0019.1>, 2017.
- Langhans, W. and Romps, D. M.: The origin of water vapor rings in tropical oceanic cold pools, *Geophysical Research Letters*, 42, 7825–7834, 2015.
- Li, X. and Srivastava, R. C.: An analytical solution for raindrop evaporation and its application to radar rainfall measurements, *J. Appl. Meteor.*, 40, 1607–1616, 2001.
- 710 Löhnert, U. and Crewell, S.: Accuracy of Cloud Liquid Water Path from Ground-Based Microwave Radiometry 1. Dependency on Cloud Model Statistics, *Radio Sci.*, 38, 8041, <https://doi.org/10.1029/2002RS002654>, 2003.
- Maahn, M., Burgand, C., Crewell, S., Gorodetskaya, I. V., Kneifel, S., Lhermitte, S., Tricht, K. V., and van Lipzig, N. P.: How does the spaceborne radar blind zone affect derived surface snowfall statistics in polar regions?, *Journal of Geophysical Research*, 119, 14,604—13,620, <https://doi.org/10.1002/2014JD022079>, 2014.
- 715 Nuijens, L., Serikov, I., Hirsch, L., Lonitz, K., and Stevens, B.: The distribution and variability of low-level cloud in the North Atlantic trades, *Quarterly Journal of the Royal Meteorological Society*, 140, 2364–2374, 2014.
- Nuijens, L., Medeiros, B., Sandu, I., and Ahlgrimm, M.: The behavior of trade-wind cloudiness in observations and models: The major cloud components and their variability, *Journal of Advances in Modeling Earth Systems*, 7, 600–616, 2015.
- Reiche, C. H. and Lasher-Trapp, S.: The minor importance of giant aerosol to precipitation development within small trade wind cumuli  
720 observed during RICO, *Atmospheric research*, 95, 386–399, 2010.
- Romps, D. M.: Exact Expression for the Lifting Condensation Level, *Journal of the Atmospheric Sciences*, 74, 3891 – 3900, <https://doi.org/10.1175/JAS-D-17-0102.1>, 2017.
- Rosenfeld, D. and Mintz, Y.: Evaporation of Rain Falling from Convective Clouds as Derived from Radar Measurements, *Journal of Applied Meteorology*, 27, 209–215, [https://doi.org/10.1175/1520-0450\(1988\)027<0209:eorffc>2.0.co;2](https://doi.org/10.1175/1520-0450(1988)027<0209:eorffc>2.0.co;2), 1988.
- 725 Schimmel, W., Kalesse-Los, H., Maahn, M., Vogl, T., Foth, A., Garfias, P. S., and Seifert, P.: Identifying cloud droplets beyond lidar attenuation from vertically-pointing cloud radar observations using artificial neural networks, *Atmospheric Measurement Techniques*, <https://doi.org/10.5194/amt-2022-149>, 2022.
- Schlemmer, L. and Hohenegger, C.: The formation of wider and deeper clouds as a result of cold-pool dynamics, *Journal of the Atmospheric Sciences*, 71, 2842–2858, 2014.
- 730 Snodgrass, E. R., Di Girolamo, L., and Rauber, R. M.: Precipitation characteristics of trade wind clouds during RICO derived from radar, satellite, and aircraft measurements, *Journal of Applied Meteorology and Climatology*, 48, 464–483, 2009.
- Stevens, B., Farrell, D., Hirsch, L., Jansen, F., Nuijens, L., Serikov, I., Brüggemann, B., Forde, M., Linne, H., Lonitz, K., et al.: The Barbados Cloud Observatory: Anchoring investigations of clouds and circulation on the edge of the ITCZ, *Bulletin of the American Meteorological Society*, 97, 787–801, 2016.
- 735 Stevens, B., Bony, S., Brogniez, H., Hentgen, L., Hohenegger, C., Kiemle, C., L'Ecuyer, T. S., Naumann, A. K., Schulz, H., Siebesma, P. A., Vial, J., Winker, D. M., and Zuidema, P.: Sugar, gravel, fish and flowers: Mesoscale cloud patterns in the trade winds, *Quarterly Journal of the Royal Meteorological Society*, 146, 141–152, <https://doi.org/10.1002/qj.3662>, 2019.
- Stevens, B., Bony, S., Farrell, D., Ament, F., Blyth, A., Fairall, C., Karstensen, J., Quinn, P. K., Speich, S., Acquistapace, C., et al.: EUREC 4 a, *Earth System Science Data*, 13, 4067–4119, 2021.

- 740 Touzé-Peiffer, L., Vogel, R., and Rochetin, N.: Cold Pools Observed during EUREC4A: Detection and Characterization from Atmospheric Soundings, *Journal of Applied Meteorology and Climatology*, 61, 593–610, <https://doi.org/10.1175/JAMC-D-21-0048.1>, 2022.
- Tridon, F., Battaglia, A., and Watters, D.: Evaporation in action sensed by multiwavelength Doppler radars, *Journal of Geophysical Research: Atmospheres*, 122, 9379–9390, 2017.
- Tukiainen, S., O'Connor, E., and Korpinen, A.: CloudnetPy: A Python package for processing cloud remote sensing data, *J. Open Source Software*, 5, 2123, <https://doi.org/10.21105/joss.02123>, 2020.
- 745 Valdivia, J. M., Gatlin, P. N., Kumar, S., Scipión, D., Silva, Y., and Petersen, W. A.: The GPM-DPR Blind Zone Effect on Satellite-Based Radar Estimation of Precipitation over the Andes from a Ground-Based Ka-band Profiler Perspective, *Journal of Applied Meteorology and Climatology*, 61, 441–456, <https://doi.org/10.1175/jamc-d-20-0211.1>, 2022.
- van der Velden, E.: CMasher: Scientific colormaps for making accessible, informative and 'cmashing' plots, *The Journal of Open Source Software*, 5, 2004, <https://doi.org/10.21105/joss.02004>, 2020.
- 750 Vial, J., Vogel, R., Bony, S., Stevens, B., Winker, D. M., Cai, X., Hohenegger, C., Naumann, A. K., and Brogniez, H.: A new look at the daily cycle of trade wind cumuli, *Journal of advances in modeling earth systems*, 11, 3148–3166, 2019.
- Vogel, R., Konow, H., Schulz, H., and Zuidema, P.: A climatology of trade-wind cumulus cold pools and their link to mesoscale cloud organization, *Atmospheric Chemistry and Physics*, 21, 16 609–16 630, <https://doi.org/10.5194/acp-21-16609-2021>, 2021.
- 755 Vogl, T., Maahn, M., Kneifel, S., Schimmel, W., Moisseev, D., and Kalesse-Los, H.: Using artificial neural networks to predict riming from Doppler cloud radar observations, *Atmospheric Measurement Techniques*, 15, 365–381, <https://doi.org/10.5194/amt-15-365-2022>, 2022.
- Witthuhn, J., Röttenbacher, J., and Kalesse-Los, H.: Virga-Sniffer (v1.0.0), <https://doi.org/10.5281/zenodo.7433405>, 2022.
- Xie, X., Evaristo, R., Troemel, S., Saavedra, P., Simmer, C., and Ryzhkov, A.: Radar observation of evaporation and implications for quantitative precipitation and cooling rate estimation, *Journal of Atmospheric and Oceanic Technology*, 33, 1779–1792, 2016.